



universität
wien

MASTERARBEIT

Titel der Masterarbeit

„Position readout of an optically trapped nano sphere in a hollow core photonic crystal fiber as a step towards parametric feedback cooling “

Verfasser

Julian Valentin Fesel, B.Sc.

angestrebter akademischer Grad

Master of science (M.Sc.)

Wien, 2014

Studienkennzahl lt. Studienblatt:

A 066 876

Studienrichtung lt. Studienblatt:

Physik

Betreuerin ODER Betreuer:

Univ.-Prof. Dr. Markus Aspelmeyer

Abstract

Optically levitated nano spheres show great prospects for the goal of preparing mesoscopic objects in their quantum mechanical ground state (Chang et al., 2010). This requires to trap the particles at pressures below 10^{-7} mBar, and hence sophisticated loading mechanisms that comply with an ultra high vacuum (UHV) environment. In (Grass, 2013) it is shown, that hollow core photonic crystal fibers (HCPCF) do not only support the trapping and transport of nano particles, but can also be used to bridge pressure differences of nine orders of magnitude, thereby making them a promising candidate for an UHV compatible loading mechanism.

The work in this thesis continues the efforts in that direction. So far the HCPCF loading scheme is limited by the fact, that due to up to now unknown reasons, the particles are lost during the evacuation at pressures around 1mBar. Active cooling of the particle motion based on parametric feedback, is known to be a working countermeasure (Gieseler et al., 2012; Li et al., 2011) and is what we set out to implement in our loading scheme. En route to this, we successfully demonstrate a three dimensional position readout of the particle motion *inside* the HCPCF, that is based on higher order guided modes. It turns out, that these modes can also have an interesting effect on the trapping potential, which is experimentally verified. In addition we discuss preliminary results on feedback cooling in one of the radial dimensions.

Acknowledgements

It is impossible to write and prepare a work like this on ones own, not to mention the experiment itself. Therefore I hope, that at least some of the people who helped me finishing this thesis, take delight in finding their names in this section along with “**best wishes and many thanks**”.

Since I am scared of running into trouble by creating a certain order in the listing (and therefore assigning a subjective quantity to their helpfulness), I decided to list the people alphabetically. I want to thank:

Markus Aspelmeyer: For giving me the chance of working in his group and writing my master’s thesis about an interesting and exciting subject.

Florian Blaser: For always taking the time to answer my questions and especially for being *very good* and knowledgeable, and able to explain things in an easy manner to others.

Uros Delic: For sharing his knowledge and explaining things, as well as a number of strange conversations.

Martin Fuchs: For his inspiring and interesting teaching in high school, which caused me to study physics.

David Grass: For being a great coworker, not being too annoyed when I made things wrong/broke them, and of course for all the time it took him to give me advice and explain things. He should also get a price for being the anti-hippie of the group.

Nikolai Kiesel: For his leadership of the trappers subgroup, many lengthy and stimulating discussions and arguments, helpful advice and especially for playing the role of the “bad cop”, who asks annoying questions about what and why we are doing things.

All the other optomechanics: Because they are friendly, open minded people and always ready to help.

My parents: For the financial support and always believing in me.

Table of Contents

1. Introduction	6
1.1. The Motivation Behind the Experiment	6
1.2. Simple Sketch and Overview of the Setup	8
2. Optical Forces and Optical Trapping	13
2.1. Maxwell's Stress Tensor and a General Expression for EM Forces	13
2.2. The Dipole Approximation	14
2.3. Guided Modes in the Hollow Core Photonic Crystal Fiber	15
2.4. Forces by a Single Propagating LP_{01} Beam	18
2.5. Forces by a Standing Wave of two LP_{01} Beams	20
2.5.1. Effects of an Imbalance in the Powers of the Beams	21
2.5.2. Translation of the Standing Wave	23
2.6. Effects of Copropagating Higher Order Modes	23
3. Monitoring the Motion of the Particle	27
3.1. Coupling of the Particle Radiation to the Guiding Modes	27
3.1.1. Description of the Light Radiated by the Particle	28
3.1.2. Calculation of the Mode Overlap	29
3.2. Detection of the Particle Motion	31
3.2.1. Detection of the Radial Motion	31
3.2.2. Detection of the Axial Motion	34
4. Center of Mass Motion, Parametric Feedback and Experimental Results	37
4.1. Brownian Motion of a Free Particle	37
4.1.1. Pressure Dependence of the Damping	38
4.2. Brownian Motion of a Particle in an Optical Potential	38
4.2.1. Powerspectrum of a Trapped Particle	39
4.3. Calculation of the Trap Frequencies	40
4.4. Experimental Timetraces and Power Density Spectra	41
4.4.1. Typical Example of Readout Data	41
4.4.2. Pressure dependence of the Damping Constant	44
4.4.3. Power dependence of the Oscillation Frequency	45
4.4.4. Spatial Beating Pattern of the Trapping Potential	46
4.5. Damping by Active Feedback on the Optical Potential	51
4.5.1. Formal Description	51
4.5.2. Experimental Results	52
5. Summary and Outlook	56
A. Appendix	57
A.1. Optical Forces	57
A.1.1. Maxwell Equations	57
A.1.2. Products of Harmonic Fields	57

A.1.3. Dipole Approximation	57
A.1.4. Modes of Free Space Propagation and the Gaussian Beam	58
A.2. Correlation and Autocorrelation Function	60
A.3. Datasheet on the Hollow Core Fiber	61
B. Zusammenfassung	62
C. Curriculum Vitae	62

1. Introduction

1.1. The Motivation Behind the Experiment

Humans are obsessed with cats. They are the all-time stars of the internet, they are always on your Facebook start page, and in Austria in the year 2012 there were around 1.7 million cats on 3.7 million households. In other words: you cannot escape them¹ (FEDIAF, 2012; Statistik Austria, 2014). Therefore it is not surprising, that from the whole range of possible animals to choose from, Erwin Schrödinger chose a cat, to be the main actor in his famous illustration of the superposition phenomenon in quantum mechanics. And since then, also physicists are obsessed with cats. One of the great unanswered questions about quantum mechanics is, whether the paradox of Schrödinger’s cat is actually true, i.e.: is it possible to prepare objects of arbitrary mass and complexity in a superposition state?

While until today there is no evidence that would negate this question, there is a certain desire for a physical effect that would, in order to tackle the so called *measurement problem* of quantum mechanics. The problem arises, because there are effectively two kinds of time evolution in the formalism: one that describes the normal evolution of an isolated system via an unitary operator, and one that describes a measurement on this system by an independent, macroscopic observer—also called *collapse of the wave function*. If one considers now the system together with the observer as the isolated system, in order to be consistent, it should be possible to achieve the results from the previous measurement process, just by evolving the composite system with standard unitary evolution. This evolution though, can just result in an entangled and superposed state of system and observer, in which every possible “measured state of the system” is correlated with the observer being in the state of “having measured this system state”. It is therefore unclear, how this result is connected with the apparent reality of a measurement in a laboratory (Penrose, 1996; Ghirardi et al., 1990).

The quantum mechanical formalism therefore relies on the possibility, to define a real and independent observer who stays in a classical state during a measurement, or in other words, who is not affected by the laws of quantum mechanics. There are several theoretical speculations about physical effects and extensions of quantum mechanics, that would result in mass limits for non-local and non-classical effects. Those include non-linear terms in the Schrödinger equation, which arise from gravitational self-interaction (Giulini and Groß ardt, 2011), collapse models that include general relativistic effects (Penrose, 1996) and models that achieve decoherence for macroscopic objects, through so called *continuous spontaneous localization* (Ghirardi et al., 1990).

On the experimental side, two important branches try to shed light on the question of quantum effects in macroscopic objects. One is matter wave interferometry with molecules of ever increasing mass, where non-classical interference effects have already been observed for molecules with masses up to 6910u (Hornberger et al., 2012; Gerlich et al., 2011). The other branch is constituted by optomechanical experiments. In these experiments one studies the interaction of light with mechanical resonators, that cover

¹While I wrote this, a cat was watching me from the other side of the sofa.

a mass range from the gram to zepto-gram scale. Just like the mass range, the different kinds of physical implementations are vast and amongst others include Fabry-Perot cavities with a suspended mirror, suspended waveguides, suspended photonic crystal cavities and levitated nano-objects (Aspelmeyer et al., 2013). The goal is, to use light to control the motion of well isolated, macro- or mesoscopic resonators, and thereby enable cooling to the ground state or the preparation of non-classical states. For electromechanical devices this was already demonstrated in (Teufel et al., 2011; O’Connell et al., 2010; Palomaki et al., 2013), and for an optomechanical device in (Chan et al., 2011).

The experiment that is described in this thesis, builds on the work that was already done by David Grass (Grass, 2013), and is part of a bigger optomechanical experiment, that is trying to cool the center of mass motion of an optically levitated silica nano-sphere to the ground state (Kiesel et al., 2013; Chang et al., 2010; Romero-Isart et al., 2010; Barker and Shneider, 2010). In comparison to other optomechanical devices, levitated objects have the advantage of strongly suppressed clamping losses. In order to reach the quantum mechanical ground state, it is necessary to trap the nano-spheres at pressures around 10^{-7} mBar. The established procedure to load particles into the trap is to evaporate a solution of the particles with an ultrasonic nebulizer, and then flood the trapping chamber with the aerosol. This is clearly incompatible with requirements of ultra high vacuum equipment, since it leads to a contamination of the chamber. It is therefore necessary, to develop a clean loading mechanism.

In (Grass, 2013) it is shown, that one can use hollow core photonic crystal fibers (HCPCF) (Russell, 2006), to bridge pressure differences of nine orders of magnitude between, and that it is possible to trap and move nano particles using the guided light in the fiber. These two properties are exactly what one needs for a loading mechanism, that can be used in a cavity cooling experiment. The goal is, to trap a particle at roompressure on one side of the fiber, and evacuate while parametrically cooling the particle, in order to reach pressures which are compatible with an uhv environment. Then the particle can be moved to the other side of the fiber, where one hands it over to the cavity cooling experiment in a second chamber, which is all the time kept at lower pressure, to protect the mirrors from pollution. Besides being a clean and pollution free particle source, this also allows controlling the loading position in the cavity, and the number of particles that are loaded².

For so far unknown reasons though, the particles escape in the millibar range during the evacuation process. A known countermeasure to this effect, is to cool the particle motion during the evacuation via parametric feedback (Li et al., 2011; Gieseler et al., 2012), and it is also known, that even without applied cooling the particles can be stably trapped lower pressures $\lesssim 10^{-3}$ mBar (Novotny). The work of this thesis, is mainly concerned with the creation of a three dimensional readout of the particle motion inside of the HCPCF. The information on the particle position can then be used for parametric feedback cooling, for which we discuss the preliminary results of an implementation in one dimension.

²Excluding the case of clustered particles.

1.2. Simple Sketch and Overview of the Setup

At first we give an overview of what is done in the experiment, and how the different parts are connected to each other. Details on relevant physical effects, experimental results and the theoretical background will be given in the later sections.

Optical Trap and Loading of the Particles

In our setup, we want to show as a proof of principle, that a readout of the particle motion in the HCPCF is possible, and that this can be used for parametric cooling and bridging of the “particle loss regime”. Therefore, the heart of the setup consists of two vacuum chambers (see green colored area in fig. 1), which are operated by the same vacuum pump and are therefore always at equal pressures (see figure 2). They are connected by a HCPCF, which is mounted in ceramic ferrules and glued into the chambers on either side. Via lenses outside the chambers, two counter propagating laser beams of equal frequency and power, are coupled through windows into the HCPCF, thereby forming a standing wave intensity pattern.

In addition to the vacuum pump connections, one chamber—which will be denoted as loading chamber (LC) and the remaining one as science chamber (SC)—is also attached to a valve controlled pipe, which leads to a small box containing an ultrasonic nebulizer. The latter is filled with a solution of silica nano spheres (the used size in this thesis is always 300nm in diameter, but can be varied if needed) in isopropanol. In section 2 it will be explained, that dielectric particles in electromagnetic fields experience a force due to an induced dipole, that draws them toward the intensity maxima of the field, thereby allowing to trap them at these positions. To do so, both chambers are evacuated down in the millibar range and the connection to the pump closed. Then the valve to the nebulizer box is slowly opened, which sucks the vapor and the silica particles into the LC. Even though one might expect a more complicated mechanism, this is all that is needed to occasionally trap particles at the entrance of the HCPCF in one of the maxima of the standing wave.

Trapping Beam Preparation and Control

The trapping laser is operated at 20W, and has a wavelength of 1064nm (see orange colored area in fig. 1). After going through a Faraday isolator to protect the laser from back reflected light, it is split up in equal parts with a polarizing beam splitter (PBS). Depending on which way they are going through the HCPCF, they will be referred to as either clockwise or counterclockwise propagating beam (CPB or CCPB). In order to be able to control the power of each beam separately, they are then sent through acousto optic modulators (AOM). Besides allowing control over the trapping potential depth via the beam power, these make it possible to shift the frequency of one of the beams by increments/decrements of 10kHz. Using this, one can move the entire standing wave in either CPB or CCPB direction and thereby change the position of the particle in Z-direction in the HCPCF (see section 2.5.2 for details).

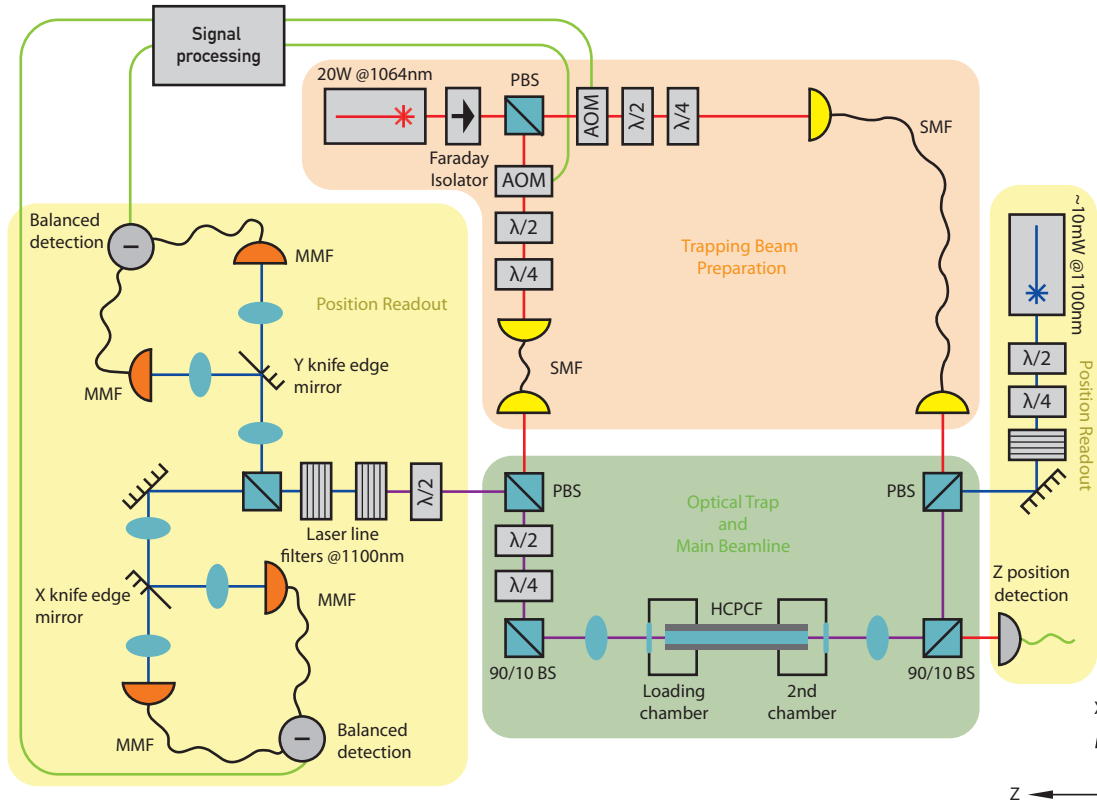


Figure 1: Scheme of the experimental setup. The orange area denotes elements required for the emission and preparation of the two trapping beams, which form a standing wave inside the HCPCF in the green area. Both beams pass through AOMs, which allow a modulation of the power and frequency, and are mode filter by the SMFs. The green area depicts the main trapping setup, including the HCPCF and the vacuum chambers, and merges the readout and trapping lasers. All elements in the yellow area concern the particle position readout. Except for the photodetector on the lower right side, all the elements are used for the radial readout. It consist of a separate laser, that is merged with the trapping laser, passes through the HCPCF and is then separated from TL via a PBS and two laser line filters. The beam is then doubled, split in half for orthogonal directions, which are then analyzed by a balanced detection. Optical elements of minor importance were left out. Meaning of the abbreviations: TL=trapping laser, RL=readout laser, PBS=Polarizing beam splitter, AOM=acousto optic modulator, SMF= single mode fiber, MMF=Multi mode fiber, HCPCF=hollow core photonic crystal fiber.

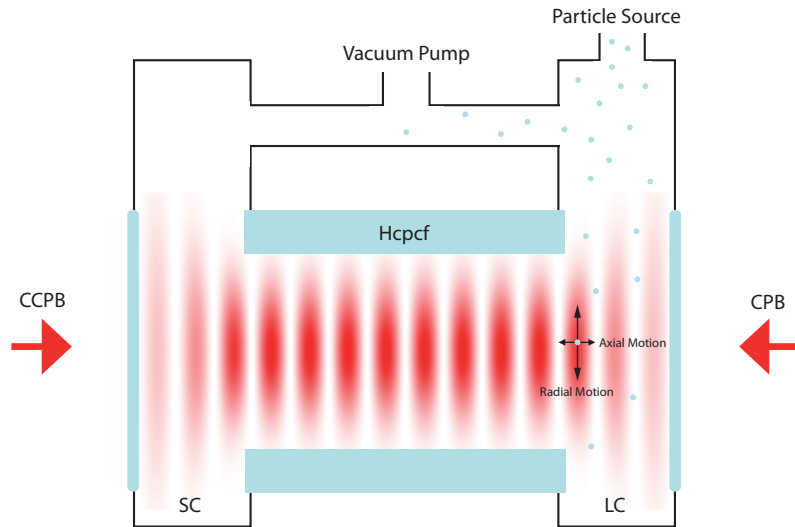


Figure 2: Scheme of the loading process. Both vacuum chambers (denoted as SC=science chamber and LC=loadingchamber) are operated by a single vacuum pump, and are therefore at the same pressure level. The trapping lasers are coupled into the hollow core photonic crystal fiber (HPCF) through two windows in the chambers, thereby creating a standing wave. Via an additional valve operated connection, a particle containing vapor can be sucked into the LV, allowing for particles to be trapped in the intensity maxima of the standing wave at the entrance of the HCPCF.

Since the mode that is coming out of the laser is not entirely gaussian, the beams are then sent through single mode fibers (SMF), which means we are effectively using them as mode filters. The PBSs that follow, are used to couple the laser that is used for the optical position readout into the main beam line. Besides that they do also enforce equal polarization of both trapping beams at this point. To maximize the transmission, the $\lambda/2$ and $\lambda/4$ plattes in front of the SMF are used. Depending on the direction they are going through the HCPCF, both trapping beams experience different polarization shifts, while for maximal interference and therefore an optimal standing wave/trapping potential, it is necessary that they have the same polarization at every point. To ensure this, additional λ plates are put in the beampath of only the CCPB. The 90/10 beam splitters, which reflect 90% and transmit 10% of the light, allow access to the light directly after the HCPCF, and also enable monitoring of the axial particle motion.

Monitoring the Particle Motion

The details of the particle motion readout will be discussed in section 3. For the motion in the Z direction, it is sufficient to just monitor the interference pattern of the trapping laser with the light that is scattered from the particle, using an optical detector. This is shown in the right lower corner of figure 1.

Monitoring the radial motion of the particle turns out to be more difficult. The light that the particle scatters from the laser, is coupled to the guiding modes of the HCPCF. Depending on the radial displacement of the particle, a varying amount of light excites a certain higher order mode with an asymmetric spatial shape. The information on the radial particle position, is therefore stored in the interference of this higher order mode with the light that is transmitted through the HCPCF. Due to the spatial asymmetry of the mode, this information can be readout of the resulting interference pattern by a spatial split detection.

The readout of the radial motion is done with a second laser, at a different wavelength of 1100nm, in order to be able to separate it from the TL more efficiently. This is necessary, since as soon as the parametric cooling is startet, one would get unwanted noise in the monitored signal from the applied modulation on the trapping laser. The separation is done by using an orthogonal polarization for the readout laser (RL) combined with a PBSs, as well as laser line filters (LLF) at 1100nm. This is illustrated in figure 1 with two colors (red=trapping, blue=readout) for the separate lasers, and a violett line wherever they are mixed. A yellow background is used to highlight the elements which are concerning the position readout. The first LLF directly after the RL head merely acts as a substitute for a Faraday isolator. The LLFs are necessary, because the trapping laser (TL) has a much greater power—around 0.6–1W in the HCPCF—than the RL, and since the separation at the PBS does not work perfectly, there is always some unwanted light from the TL reflected at the PBS. This “garbage light” is usually in the same power range as the RL, and would therefore cause considerable noise in the readout.

After the separation, the RL is split in two equal parts using a $\lambda/2$ plate and a PBS. Both beams are then spatially cut in half by a knife edge mirror. This is a mirror with

a sharp edge, that is put half way into the beam, thereby deflecting one half in another direction while the other is unaltered. This is done for one beam in X and for the other in Y direction. Both halves for both beams are then coupled into multi mode fibers (MMF), which separately for X and Y lead to balanced detectors. There, the powers in both halves are measured, then subtracted from each other and finally given out as a voltage signal.

Although for the sake of clarity not explicitly shown in fig. 1, the knife edge mirrors are mounted on piezo crystals, which are locked to the error signal of the balanced beam halves. This is necessary, because the HCPCF mount in the ferrule leaves room for slight movements, and thereby causes the beam to jitter. By focusing the beam on the knife edge mirrors, it becomes small enough as that the small range of the piezo crystals is sufficient to counteract the shifts of the beam.

Cooling of the Particle Motion

The details of the parametric cooling will be discussed in chapter 4. In axial direction, escaping from the trap is unlikely for a particle somewhere inside the HCPCF, since it will only move in the next maxima of the standing wave. Therefore, only cooling the radial motion of the particle should be sufficient for our goal of reaching low pressures.

In order to cool the motion, one must apply an opposing force on the particle, whenever it moves outward of the trapping potential. This can be done by simply increasing the power of the TL, which leads to a stiffer potential and therefore to an inward pointing force. The needed modulation of the potential for a specific motion of the particle, can be calculated from the monitoring signal, which is in our case done with an FPGA signal processing unit. The modulation is then simply applied to the TL using the AOMs.

2. Optical Forces and Optical Trapping

When one thinks about electromagnetic forces, it is natural to imagine charged particles or objects, that interact with each other by the laws of electromagnetism. At first sight it therefore seems surprising, that optical light i.e. electromagnetic waves can also exert significant forces on neutral particles and atoms.

These forces were first described by A. Ashkin in 1970 (Ashkin, 1970a,b) and today the field of optical trapping is vast and still active (Marago et al., 2013). Although neutral atoms and particles have a net charge of zero, their constituents (electrons and protons) do not, which makes all the difference for their interaction with light. The forces then arise due to scattering of light (called *scattering forces*) and induced polarization in the particles (called *gradient forces*). We will now take a closer look on the origin and characteristic properties of those two kinds of forces, and derive quantitative expressions for their description.

2.1. Maxwell's Stress Tensor and a General Expression for EM Forces

Using the formula for the Lorentz force $\mathbf{F} = q\mathbf{E} + \mathbf{j} \times \mathbf{B}$ and the Maxwell equations (see appendix A.1.1), one can derive a relation that manifests conservation of momentum for electromagnetic fields and the charges they are acting on (Jackson, 1999)³:

$$\int_V \nabla \cdot \mathbf{T} dV = \frac{d}{dt} \frac{1}{c^2} \int_V (\mathbf{E} \times \mathbf{H}) dV + \int_V (q\mathbf{E} + \mathbf{j} \times \mathbf{B}) dV \quad (1)$$

Where \mathbf{T} is a matrix that is called *Maxwell's stress tensor* and is given by:

$$T_{ij} = (\epsilon_0 \epsilon E_i E_j + \mu_0 \mu H_i H_j) - \frac{1}{2} (\epsilon_0 \epsilon E^2 + \mu_0 \mu H^2) \delta_{ij} \quad (2)$$

Using the fact that the integral of a divergence over a volume is equal to an integration over the bounding surface, we can recast (1) into:

$$\oint_S \mathbf{T} \cdot d\mathbf{n} = \frac{d}{dt} (\mathbf{P}_{\text{field}} + \mathbf{P}_{\text{mech}}) \quad (3)$$

Where \mathbf{P}_{mech} denotes the total momentum of the charges and $\mathbf{P}_{\text{field}}$ the total momentum of the electromagnetic field, which is proportional to the *Pointing vector*:

$$\mathbf{P}_{\text{field}} = \frac{1}{c^2} (\mathbf{E} \times \mathbf{H}) = \frac{1}{c^2} \mathbf{S} \quad (4)$$

The timescale at which the amplitude of light changes at optical frequencies, is much smaller than any movement of the particles. Therefore, to make things easier, one looks at the time average of the involved forces. If we consider only harmonic fields, i.e. fields of the form $\mathbf{E}(\mathbf{r}, t) = \text{Re}\{\tilde{\mathbf{E}}(\mathbf{r})e^{-i\omega t}\}$ ⁴, then the Pointing vector has only a constant plus

³For better readability, the arguments of the fields are omitted: $\mathbf{E}(\mathbf{r}, t) = \mathbf{E}$

⁴In the following we will use the tilde to denote the complex and time independent amplitude.

a harmonic dependence on time (see appendix A.1.2), and therefore the time average of the derivative vanishes. This leaves us with a general expression for the mechanical force:

$$\langle \mathbf{F}_{\text{mech}} \rangle = \oint_S \langle \mathbf{T} \rangle \cdot d\mathbf{n} \quad (5)$$

It is important to note, that the fields forming the stress tensor are the fields of the total system. In the case of a glass bead in a laser beam, those are the field of the laser beam and the field that describes the light that is scattered from the bead. Calculating the forces with this method, therefore means first solving the Maxwell equations for a given system, then deriving the stress tensor from the fields and finally performing the surface integration. Since it is obvious, that even for a simple system this is no easy task, we will now have a look at an approximated model.

2.2. The Dipole Approximation

In the case that the particle is much smaller than the wavelength of the light, it can be approximated as a point dipole, which is the usual treatment in the field (Chang et al., 2010; Romero-Isart et al., 2010; Barker and Shneider, 2010). It can be shown, that the force of an arbitrary field on a point dipole is given by (Novotny and Hecht, 2006):

$$\mathbf{F}_{\text{dip}} = (\mathbf{p} \cdot \nabla) \mathbf{E} + \dot{\mathbf{p}} \times \mathbf{B} + \dot{\mathbf{r}} \times (\mathbf{p} \cdot \nabla) \mathbf{B} \quad (6)$$

Where \mathbf{p} is the electric dipole moment and \mathbf{r} is the center of mass position of the particle. Since the particle motion is much slower than c , we can neglect the last term in this expression. To get an expression for the average, we first note that without the third term, (6) can be rewritten as (see appendix A.1.3):

$$\mathbf{F}_{\text{dip}} = \sum_i p_i \nabla E_i + \frac{d}{dt} (\mathbf{p} \times \mathbf{B})$$

As in the preceding section, if we consider harmonic fields the second term vanishes under the time average, which leaves us with:

$$\langle \mathbf{F}_{\text{dip}} \rangle = \sum_i \langle p_i \nabla E_i \rangle \quad (7)$$

In the case of a glass bead, one can assume linear and isotropic polarizability, which can mathematically be expressed as a relation between the complex amplitudes of the harmonic fields: $\tilde{\mathbf{p}} = \alpha \tilde{\mathbf{E}}$, where α is a complex number. Using this, the relation for products of harmonic fields (appendix A.1.2) and rewriting the complex amplitude of the electric field as $\tilde{\mathbf{E}}(\mathbf{r}) = |\tilde{\mathbf{E}}(\mathbf{r})| e^{i\phi(\mathbf{r})} \hat{\mathbf{n}}$, we can rewrite the last equation:

$$\begin{aligned} \langle \mathbf{F}_{\text{dip}} \rangle &= \sum_m \langle p_m \nabla E_m \rangle = \frac{1}{2} \sum_m \text{Re} \left\{ (\alpha \tilde{E}_m)^* \nabla \tilde{E}_m \right\} \\ &= \frac{1}{2} \sum_m n_m^2 \text{Re} \left\{ \alpha^* |\tilde{\mathbf{E}}(\mathbf{r})| e^{-i\phi(\mathbf{r})} \left(e^{i\phi(\mathbf{r})} \nabla |\tilde{\mathbf{E}}(\mathbf{r})| + i e^{i\phi(\mathbf{r})} |\tilde{\mathbf{E}}(\mathbf{r})| \nabla \phi(\mathbf{r}) \right) \right\} \quad (8) \\ &= \frac{1}{4} \text{Re} \{ \alpha \} \nabla |\tilde{\mathbf{E}}(\mathbf{r})|^2 + \frac{1}{2} \text{Im} \{ \alpha \} |\tilde{\mathbf{E}}(\mathbf{r})|^2 \nabla \phi(\mathbf{r}) \end{aligned}$$

The first term of this result is denoted as the *gradient force*, and the second one as *scattering force*. While the former name should be self explaining, the interpretation as scattering force can be understood by looking at a running wave with the phase dependence $\phi(\mathbf{r}) = \mathbf{k} \cdot \mathbf{r}$. In this case, the scattering force is simply pointing in the direction of the wave vector of the field. For reference we restate the expressions for both forces:

$$\mathbf{F}_{\text{grad}} = \frac{1}{4} \text{Re}\{\alpha\} \nabla |\tilde{\mathbf{E}}(\mathbf{r})|^2 \quad \mathbf{F}_{\text{scatt}} = \frac{1}{2} \text{Im}\{\alpha\} |\tilde{\mathbf{E}}(\mathbf{r})|^2 \nabla \phi(\mathbf{r}) \quad (9)$$

While the gradient force points always in the direction of maximum intensity of the field, the scattering force points in the direction the wave is running. As the name already states, the gradient force can be described by and derived from a scalar potential. This potential will become important for our discussion of the forces and its explicit form is:

$$U_{\text{grad}}(\mathbf{r}) = -\frac{1}{4} \text{Re}\{\alpha\} |\tilde{\mathbf{E}}(\mathbf{r})|^2 \quad (10)$$

In order to be able to calculate the forces on a particle, we now only need an expression for the electric field, and an the value of the polarizability of a silica sphere. While the former will be discussed in the next sections, an expression for α is given in (Draine, 1988):

$$\alpha = \frac{\alpha_0}{1 - i\alpha_0 k^3 / (6\pi\epsilon_0)} \quad \alpha_0 = 4\pi\epsilon_0 a_p^3 \frac{\epsilon - 1}{\epsilon + 2} \quad (11)$$

Where k is the wave vector of the polarizing wave, ϵ_0 the vacuum permittivity and ϵ the relative permittivity of the material the particle consists of. Since it will be needed in the upcoming discussions, we explicitly state the expressions for the real and imaginary part of the complex polarizability:

$$\text{Re}\{\alpha\} = \alpha_0 \left(1 + \left(\frac{\alpha_0 k^3}{6\pi\epsilon_0} \right)^2 \right)^{-1} \quad \text{Im}\{\alpha\} = \frac{\alpha_0^2 k^3}{6\pi\epsilon_0} \left(1 + \left(\frac{\alpha_0 k^3}{6\pi\epsilon_0} \right)^2 \right)^{-1}$$

For the case that the particle radius is small compared to the wavelength, the denominator of both expression can be approximated by 1, which leaves us with:

$$\text{Re}\{\alpha\} = \alpha_0 \quad \text{Im}\{\alpha\} = \frac{\alpha_0^2 k^3}{6\pi\epsilon_0} \quad (12)$$

2.3. Guided Modes in the Hollow Core Photonic Crystal Fiber

In standard step index optical fibers, light is guided by total internal reflection in a core with a high refractive index n_{co} , that is surrounded by a material (called cladding) with lower refractive index n_{cl} . Since there is no viable material with a lower refractive index than air, using this mechanism, it would be impossible to have an optical fiber, in which the light is guided in air or vacuum.

Guidance Mechanism

In 1991 Philip Russel came up with the idea to make an optical fiber, that consist of a silica rod with a big hole—representing the core—in the middle, which is surrounded by a periodic arrangement of smaller holes, also called a photonic crystal (see figure 3b) (Russell, 2003, 2006). Similar like electronic band gaps in crystalline materials, the photonic crystal surrounding the core creates band gaps for the transverse radiation, that is, excludes certain wavevectors k_{\perp} from propagation. These gaps are visualized in so called band gap diagrams, in which the vertical axis denotes the normalized frequency $\frac{\omega\Lambda}{c}$, and the horizontal axis the normalized axial wavevector $\beta\Lambda$ of the radiation, with Λ being the lattice period of the photonic crystal. An example is given in figure 3a. The black “fingers” denote areas in which band gaps for the transverse radiation occur and can usually only be calculated in numerical simulations. If these areas extend into the regime where the size of the axial wave vector allows propagation in air, meaning that $\beta < kn_{\text{air}}$, then guidance of light in the hollow core becomes possible. In the diagram in figure 3a, one possible point is marked with P. The fiber we are using in the experiment has a band gap around 1060nm, and a core radius of $5\mu\text{m}$ (see appendix A.3 for a data sheet on the HCPCF).

Spatial Modes of the Guided Light

In (Digonnet et al., 2005; Zamani Aghaie et al., 2009) it is argued, that the modes of HCPCF have a strong resemblance to the linear polarized (LP) modes of standard step-index fibers, and it is common practice in the field, to use the LP modes and propagation constants derived in (Marcatili and Schmeltzer, 1964) for the case of a hollow cylindrical dielectric, as an approximation for calculations concerning a HCPCF (Schmidt et al., 2013; Euser et al., 2008; Nold et al., 2010).

In cylindrical coordinates, the electric fields of these modes are described by the following complex amplitudes:

$$\tilde{\mathbf{E}}_{nm}^s(r, \phi, z) = \begin{cases} \sqrt{\frac{2P}{c\epsilon_0}} \zeta_{nm} J_n \left(\frac{u_{nm}r}{a_c} \right) \cos(n\phi) e^{iz\beta_{nm}} \hat{\mathbf{n}}_{\text{pol}} & \text{for } s = 0 \\ \sqrt{\frac{2P}{c\epsilon_0}} \zeta_{nm} J_n \left(\frac{u_{nm}r}{a_c} \right) \sin(n\phi) e^{iz\beta_{nm}} \hat{\mathbf{n}}_{\text{pol}} & \text{for } s = 1 \end{cases} \quad (13)$$

$n = 0, 1, 2, \dots \quad m = 1, 2, 3, \dots$

Where ζ_{nm} is a normalization factor, P the optical power propagating in the beam, J_n are the Bessel functions of the first kind, u_{nm} is the m th root of the Bessel function J_n , a_c the core radius, $\hat{\mathbf{n}}_{\text{pol}}$ is a normalized vector that specifies the polarization of the mode, and β_{nm} is the propagation constant for the specific LP mode, which is given by the expression:

$$\beta_{nm} = \frac{2\pi}{\lambda} \left[1 - \frac{1}{2} \left(\frac{u_{nm}\lambda}{2\pi a_c} \right)^2 \right] \quad (14)$$

Where λ is the wavelength of the light in free space. For the parameters used in the setup, the difference between the wave vectors of lower order modes inside the fiber and in free space is marginal ($\frac{k}{\beta_{01}} \approx 1.003$, $\frac{k}{\beta_{11}} \approx 1.008$). Despite that, we will see in subsection

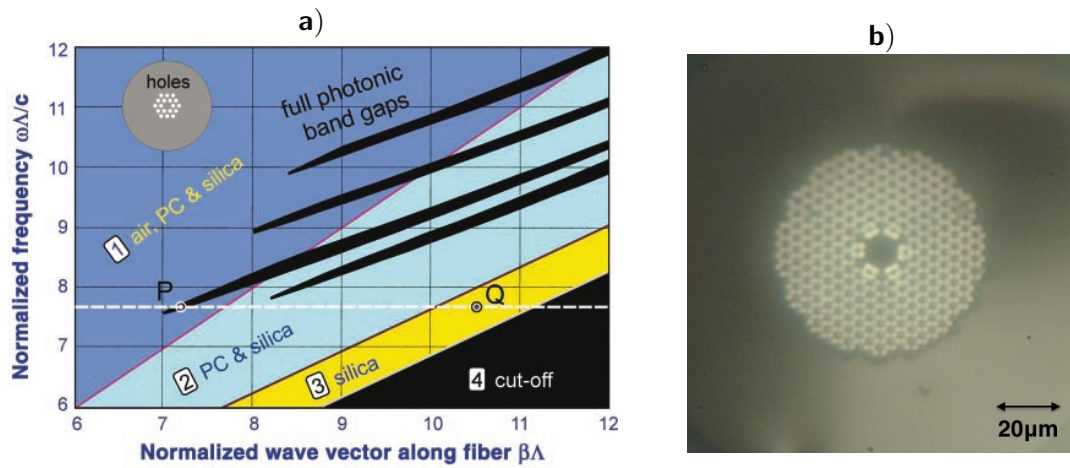


Figure 3: **a)** Example for a band gap diagram of a HCPCF. Several colored areas denote possible materials for the axial wavevector/frequency pairs, which also correspond to a certain radial wavevector. The black finger shaped regions visualize the bandgaps, in which radial propagation is prohibited. P marks a configuration, for which propagation of light in the air filled core of the HCPCF is possible, since the axial wave vector is in the “air” region and radial propagation prevented by the band gap. Taken from (Russell, 2003). **b)** Self made microscopic picture, made from the tip of the used hollow core photonic bandgap fiber *HC-1060-02* from *NKT Photonics*. The hexagonal silica structure is illuminated, while the darker spots are the holes forming the photonic crystal and the guiding core. The latter is formed by the removal of seven unit cells from the lattice.

2.6 and 3.2.1, that this difference can cause significant effects. The expression for the normalization constant ζ_{nm} can be derived from the constraint, that the integrated intensity in the core is equal to the power of the beam:

$$\zeta_{nm} = \begin{cases} \frac{1}{a_c \sqrt{\pi} J_1(u_{0m})} & \text{for } n = 0 \\ \left(\frac{-a_c^2 J_{n-1}(u_{nm}) J_{n+1}(u_{nm}) (4\pi n + \sin(4\pi n))}{8n} \right)^{-1/2} & \text{for } n \geq 1 \end{cases} \quad (15)$$

Excluding the \mathbf{E}_{0m}^s modes, for which the sinusoidal term becomes zero, all LP modes have a four fold degeneracy. Two stemming from the possible polarizations, and two from the two possible forms given in equation (13), i.e. $s = \{0, 1\}$, where the second expression represents the first rotated by $\frac{\pi n}{2}$ around the axis of propagation. The spatial forms of the amplitudes that describe the LP modes, are visualized in figure 4. Via the cosine (sine) dependence, the index n determines the number of roots in azimuthal direction, while the index m directly determines the number of roots in radial direction. The modes that will be important in our case, are the fundamental LP_{01} and the first higher order LP_{11} mode. In the discussions that follow in the next sections, we will always work with the $s = 0$ LP modes (since the orientation of the coordinate system can be chosen arbitrarily), and omit this index for better readability.

2.4. Forces by a Single Propagating LP_{01} Beam

The fundamental LP_{01} mode has a strong resemblance to the gaussian beam of a laser propagating in free space (see figure 5 and appendix A.1.4), and is the mode that the trapping and readout lasers are mainly coupled to. To get a feeling for the forces that are created by a beam in the fiber, we will now derive the gradient and scattering forces for the case that laser light is coupled into the fiber from one side. To do this, we need the following properties of the Bessel functions:

$$\frac{\partial J_n(r)}{\partial r} = \frac{1}{2} (J_{n-1}(r) - J_{n+1}(r)) \quad (16a)$$

$$J_{-n}(r) = (-1)^n J_n(r) \quad (16b)$$

And the form of the gradient in cylindrical coordinates:

$$\nabla f = \frac{\partial f}{\partial r} \hat{\mathbf{e}}_r + \frac{1}{r} \frac{\partial f}{\partial \phi} \hat{\mathbf{e}}_\phi + \frac{\partial f}{\partial z} \hat{\mathbf{e}}_z \quad (16c)$$

Gradient Force

Simply by substituting the expression for the LP_{01} mode (13) into equation (10), we can derive the potential for a single beam:

$$U_{\text{single}}(\mathbf{r}) = -\frac{\text{Pre}\{\alpha\}}{2\pi a_c^2 c \epsilon_0 J_1^2(u_{01})} J_0^2\left(\frac{u_{01} r}{a_c}\right) \quad (17)$$

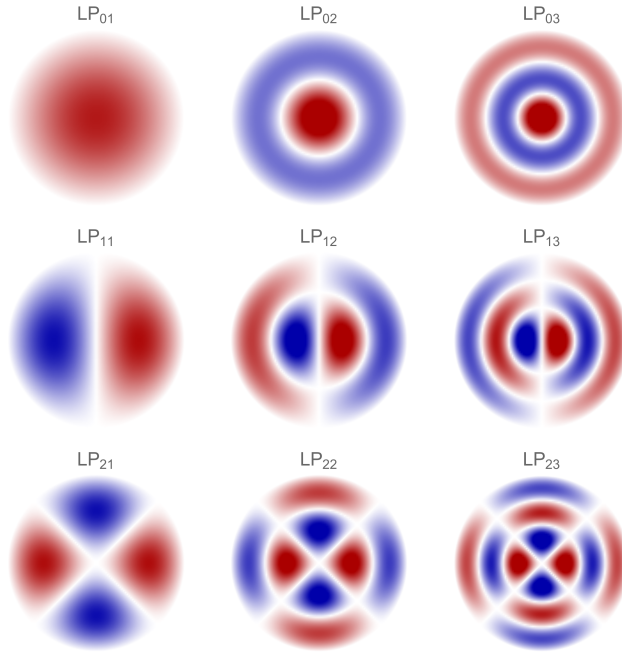


Figure 4: Plots of the amplitude of the electric field $E_{nm}^s(r, \phi)$ in the plane perpendicular to the fiber axis, for the fundamental and the first higher order LP modes ($n=\{0,1,2\}$, $m=\{1,2,3\}$, $s=0$). In order to get real values, z was set to zero. Red denotes positive and blue negative values.

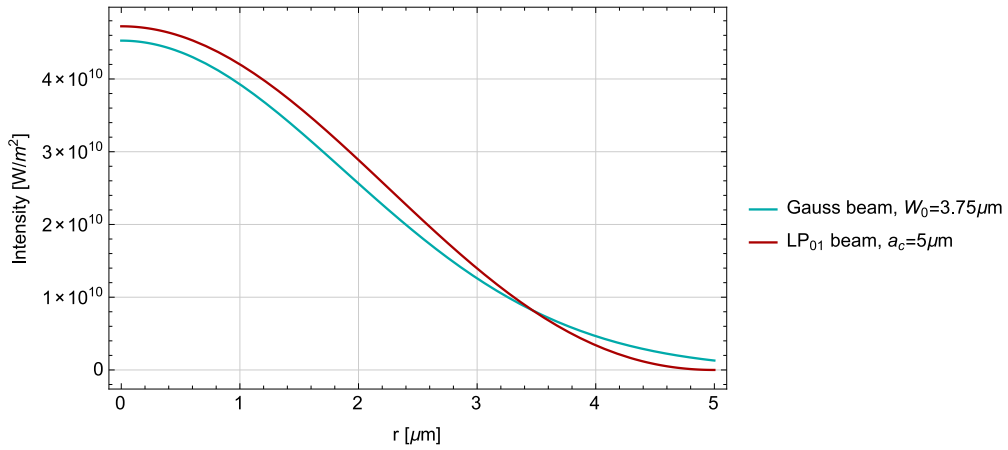


Figure 5: Comparison of the radial intensity profile of a gaussian with a waist of $W_0 = 3.75\mu\text{m}$ (as specified in the data sheet of the HCPCF A.3) and an LP_{01} beam for a core radius of $a_c = 5\mu\text{m}$. The total power propagating in each beam, was taken to be 1W.

Since this potential depends only on r , using (16c) makes it easy to calculate the force:

$$\mathbf{F}_{\text{grad}} = -\frac{P\text{Re}\{\alpha\}u_{01}}{\pi a_c^3 c \epsilon_0 J_1^2(u_{01})} J_0\left(\frac{u_{01}r}{a_c}\right) J_1\left(\frac{u_{01}r}{a_c}\right) \hat{\mathbf{e}}_r$$

Where we used the previously given relations for Bessel functions. As can be seen, in the case of a single beam, the gradient force only has a radial component, which is always directed to the center of the fiber core and therefore only provides a radial trap.

Scattering Force

For a single LP₀₁ Bessel beam, it is straightforward to read out the phase dependence from the defining equation (13): $\phi(\mathbf{r}) = \beta_{01}z$. Substituting into equation (9), the expression for the scattering force turns out to be:

$$\mathbf{F}_{\text{scatt}}(\mathbf{r}) = \frac{P\text{Im}\{\alpha\}\beta_{01}}{\pi a_c^2 c \epsilon_0 J_1^2(u_{01})} J_0^2\left(\frac{u_{01}r}{a_c}\right) \hat{\mathbf{z}} \quad (18)$$

It can be seen, that the scattering force points in the direction of beam propagation and is independent of the axial position in the fiber. The maximum force occurs in the center of the core, where also the intensity has its maximum. Including the gradient force, the effect of a single laser beam from one side is therefore to accelerate the particle in the direction of propagation, while trapping it in the center of the core.

2.5. Forces by a Standing Wave of two LP₀₁ Beams

We now discuss the situation that concerns the actual setup, of two counter propagating LP₀₁ modes with equal powers in the HCPCF. Using the definition of the LP modes, we can come up with an expression for the complex amplitude of the electric field:

$$\begin{aligned} \tilde{\mathbf{E}}_{\text{sw}}(\mathbf{r}) &= \sqrt{\frac{2P}{c\epsilon_0}} \zeta_{01} J_0\left(\frac{u_{01}r}{a_c}\right) \left(e^{i\beta_{01}z} + e^{-i\beta_{01}z}\right) \hat{\mathbf{n}}_{\text{pol}} \\ &= 2\sqrt{\frac{2P}{c\epsilon_0}} \zeta_{01} J_0\left(\frac{u_{01}r}{a_c}\right) \cos(\beta_{01}z) \hat{\mathbf{n}}_{\text{pol}} \end{aligned}$$

From this we can derive the potential of the gradient force, and the phase function of the wave:

$$U_{\text{sw}}(\mathbf{r}) = -\frac{2P\text{Re}\{\alpha\}}{\pi c \epsilon_0 a_c^2 J_1^2(u_{01})} J_0^2\left(\frac{u_{01}r}{a_c}\right) \cos^2(\beta_{01}z) \quad \phi(\mathbf{r}) = 0 \quad (19)$$

As one would intuitively expect, the vanishing phase dependence results in a vanishing scattering force for counter propagating beams with equal powers, and for the discussion of the trap we can therefore focus on the gradient force. Unlike in the case of a single beam, the potential now depends on r and z , which results in an additional force in the axial direction in contrast to the case of a single beam. Since the explicit expressions for

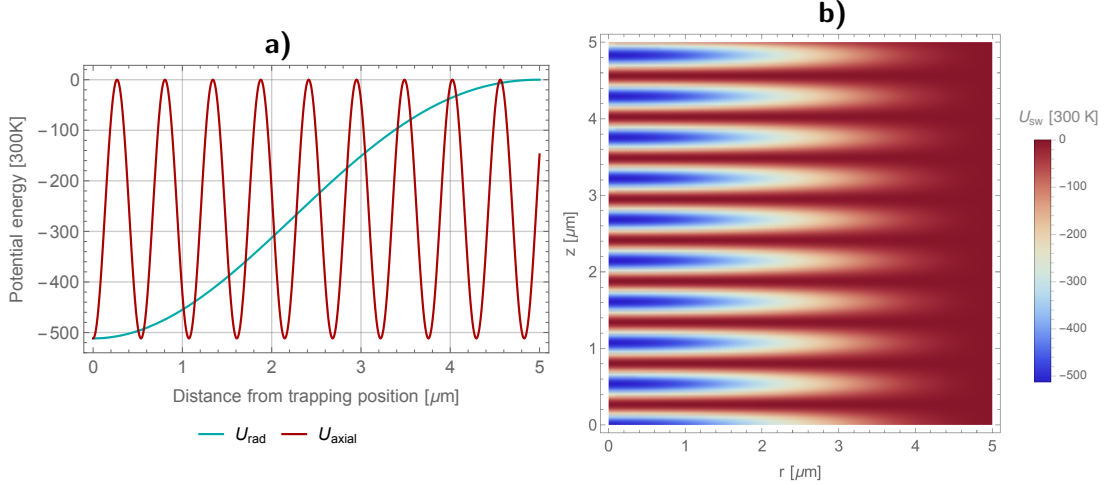


Figure 6: **a)** Comparison of the trapping potential in axial and radial direction. It can be seen, that although the depth of both traps is the same, the stiffness of the trap in axial direction is much higher than for the radial case. **b)** Density plot of the potential in the fiber. Both axes show the same length scale.

the force won't be needed, we will omit them here and discuss the properties only using the potential.

Figure 6 shows two plots to illustrate the dimensions and depth of the potential, that a particle sees in axial and radial direction. For the calculations, parameters that also occur in the experiment were used, namely a trapping beam power of 600mW, a particle radius of 150nm and a laser wavelength of 1064nm. While the depth of the potential is equal for the axial and radial direction, the stiffness in axial direction is much higher. A short calculation shows, that the full width at half minimum of the trap is approximately $\Delta z_{\text{FWHM}} \simeq \frac{\lambda}{4} = 266\text{nm}$ in axial and $\Delta r_{\text{FWHM}} \simeq 0.94a_c \approx 4.68\mu\text{m}$ in radial direction.

2.5.1. Effects of an Imbalance in the Powers of the Beams

The experimental setup allows only for a balance of the two trapping beams up to an uncertainty around 10% of the trapping beam power. Therefore we want to calculate the possible influence, that this can have on our trap. For this we assume that one beam has a power of P , while the other has a small additional offset $P(1 + \xi)$. Using the usual definitions, this leads to the following electric field:

$$\tilde{\mathbf{E}}_{\text{sw}}(\mathbf{r}) = \sqrt{\frac{2P}{c\epsilon_0}} \zeta_{01} J_0 \left(\frac{u_{01}r}{a_c} \right) \left(e^{i\beta_{01}z} + \sqrt{1 + \xi} e^{-i\beta_{01}z} \right) \hat{\mathbf{n}}_{\text{pol}} \quad (20)$$

One can instantly see, that unlike in the preceding section, this expression is not purely real, which leads to a non-vanishing phase function and therefore a scattering force. Analogous to the last subsections, we calculate the optical potential and the phase

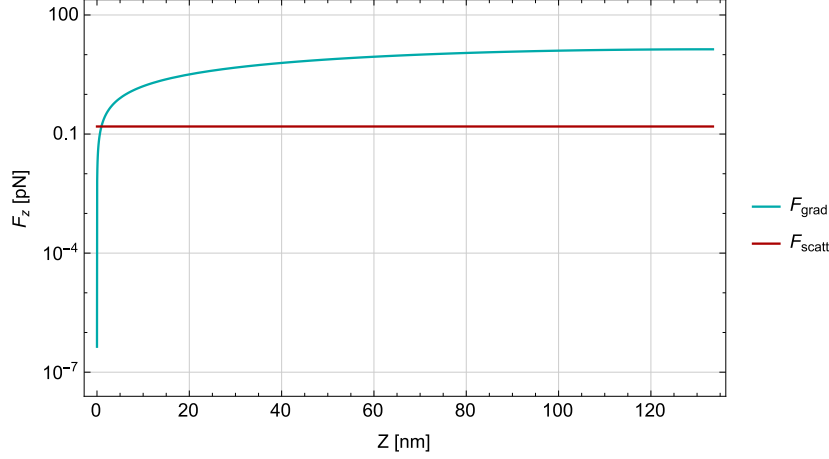


Figure 7: Logarithmic plot of the scattering and gradient force along the fiber. Particle size: $a_p = 150\text{nm}$, used beam powers: $P_{\text{cpb}} = 0.6\text{W}$, $P_{\text{ccpb}} = 0.66\text{W}$

function:

$$U_{\text{sw}}(\mathbf{r}) = -\frac{P\text{Re}\{\alpha\}}{2\pi c\epsilon_0 a_c^2 J_1^2(u_{01})} J_0^2\left(\frac{u_{01}r}{a_c}\right) \left((2 + \xi) + 2\sqrt{1 + \xi\cos(2\beta_{01}z)} \right)$$

$$\phi(\mathbf{r}) = \arctan\left(-\frac{2 + \xi - 2\sqrt{1 + \xi\cos(2\beta_{01}z)}}{\xi} \tan(\beta_{01}z) \right)$$

It seems counterintuitive that the phase function depends on the axial position z , since one would expect a constant force as in the case of a single LP_{01} mode in subsection 2.4. The final calculation of the force although shows, that the z -dependent terms from the absolute square of the electric field and the derivative of the phase function in (9) cancel, resulting in a constant scattering force in axial direction:

$$|\mathbf{F}_{\text{scatt}}(\mathbf{r})| = \frac{\text{Im}(\alpha)P\beta_{01}}{a_c^2\pi c\epsilon_0 J_1^2(u_{01})} J_0^2\left(\frac{u_{01}r}{a_c}\right) \xi \quad (21)$$

The expression for the gradient force is lengthy and will be omitted at this point.

Figure 7 shows the size of the gradient and scattering force along the fiber axis, for parameters used in the setup, a particle centered in the fiber core and an assumed imbalance of $\xi = 0.1$. Without an imbalance, the trapping position of the particle would be at $z = 0$, where the gradient force becomes zero and changes sign (not visible in a logarithmic plot). In case of an imbalance, the scattering force merely shifts the trapping position by a small amount ($\simeq 0.5\text{nm}$) in the direction of the more powerful beam, until F_{grad} and F_{scatt} are of equal size. Compared with the FWHM of the trap, this effect is therefore small enough to be neglected in the upcoming discussions.

2.5.2. Translation of the Standing Wave

As roughly described in the introduction, the AOMs allow for a slight detuning $\Delta\omega$ of the laser frequency of one of the two trapping beams. If only one of the lasers is detuned, this results in a moving interference pattern and allows the translation of the particle. In the jargon of the field, this is also denoted as a ‘‘conveyor belt’’. In order to describe this effect mathematically, it is necessary to consider the time dependent field. Since the change of the wave vector by the detuning is negligible, the electric field can be described as:

$$\mathbf{E}_{\text{detuning}}(\mathbf{r}) = \text{Re} \left\{ \zeta_{01} J_0 \left(\frac{u_{01}r}{a_c} \right) \left(e^{i\beta_{01}z} + e^{-i(\beta_{01}z + \Delta\omega t)} \right) e^{-i\omega t} \right\} \hat{\mathbf{n}}_{\text{pol}} \quad (22)$$

The used detuning in the setup is in increments of $\Delta\omega = 2\pi 10\text{kHz}$ and therefore much smaller than the optical frequency of $\omega \approx 2\pi 280\text{THz}$. For this reason, the time dependence through the $\Delta\omega$ term in (22) by the time average which we used in the derivation of the forces, and we can treat it as part of the complex amplitude. From the remaining expression one can easily calculate the optical potential:

$$U_{\text{detuning}}(\mathbf{r}) = -\frac{2P\text{Re}\{\alpha\}}{\pi c \epsilon_0 a_c^2 J_1^2(u_{01})} J_0^2 \left(\frac{u_{01}r}{a_c} \right) \cos^2 \left(\beta_{01}z + \frac{\Delta\omega}{2}t \right) \quad (23)$$

$$\stackrel{\beta_{01} \simeq k}{=} -\frac{2P\text{Re}\{\alpha\}}{\pi c \epsilon_0 a_c^2 J_1^2(u_{01})} J_0^2 \left(\frac{u_{01}r}{a_c} \right) \cos^2 \left(k \left(z + \frac{c\Delta\omega}{2\omega}t \right) \right)$$

Comparing this with the potential of a standing wave without detuning of one beam in (19), we see that this is the same expression except that the standing wave is now moving with a speed of:

$$v_{\text{sw}} = \frac{c\Delta\omega}{2\omega} \quad (24)$$

The direction of the motion is in the direction of the beam with the greater frequency. For the experimental parameters this gives $v_{\text{sw}} \approx 5 \frac{\text{mm}}{\text{s}}$ for a single increment of $\Delta\omega = 2\pi 10\text{kHz}$.

2.6. Effects of Copropagating Higher Order Modes

Even though the trapping beams coupled into the HCPCF are gaussian, imperfect coupling can result in excited higher order LP modes. In this section, we will discuss the effects that this can have on the trapping potential. For this we assume, that a certain fraction of the trapping beam power excites a LP₁₁ mode. At first we consider only a single higher order mode, and then extend the discussion to the case of two counterpropagating LP₁₁ modes.

Copropagating LP₁₁ Mode From One Side

In this case, two beams with equal powers P are coupled into the fiber. We assume, that on one side a fraction of the power $P\xi$ is coupled into a LP₁₁ mode, while the rest $P(1 - \xi)$ is still propagating in the fundamental LP₀₁ mode. To facilitate the writing,

we first introduce a new notation for the LP modes: $\tilde{\mathbf{E}}_{\text{nm}}(\mathbf{r}) = \sqrt{P} \varepsilon_{\text{nm}}(r, \phi) e^{i\beta_{\text{nm}}z} \hat{\mathbf{n}}_{\text{pol}}$. The complex amplitude of the electric field in the fiber can then be written as:

$$\tilde{\mathbf{E}}_{\text{single}}(\mathbf{r}) = \sqrt{P} \left[\varepsilon_{01}(r, \phi) \left(e^{i\beta_{01}z} + \sqrt{1-\xi} e^{-i\beta_{01}z} \right) + \varepsilon_{11}(r, \phi) \sqrt{\xi} e^{-i\beta_{11}z} \right] \hat{\mathbf{n}}_{\text{pol}} \quad (25)$$

A short calculation gives the optical potential for this configuration:

$$U_{\text{single}}(\mathbf{r}) = -\frac{\text{Re}\{\alpha\}P}{4} \left[\varepsilon_{01}^2(r, \phi) \left(2 - \xi + 2\sqrt{1-\xi} \cos(2\beta_{01}z) \right) + \varepsilon_{11}^2(r, \phi) \xi \right. \\ \left. + 2\varepsilon_{01}(r, \phi) \varepsilon_{11}(r, \phi) \left(\sqrt{\xi} \cos((\beta_{01} + \beta_{11})z) + \sqrt{\xi(1-\xi)} \cos((\beta_{01} - \beta_{11})z) \right) \right] \quad (26)$$

The first term in the bracket is the already discussed standing wave by the fundamental mode, here in the case of two slightly imbalanced beams. The second term is weighted by ξ , and has therefore only a minor and spatially symmetric contribution to the potential. A new and interesting effect is caused by the last term. The product $\varepsilon_{01}(r, \phi) \varepsilon_{11}(r, \phi)$ is spatially antisymmetric, as one can easily see by looking at the mode shapes in fig. 4. This term therefore shifts the trap away from the center of the core, in the direction of the asymmetry of the mode. There is a highly oscillatory contribution to this shift with a wavelength of $\lambda_{\text{shift1}} = \frac{2\pi}{\beta_{01} + \beta_{11}} \approx 535\text{nm}$ (highlighted in red), that is only marginally different from the wavelength of the standing wave $\lambda_{\text{sw}} = \frac{\pi}{\beta_{01}} \approx 534\text{nm}$ (highlighted in green), and a shift that happens on a larger scale, with a wavelength of $\lambda_{\text{shift2}} = \frac{2\pi}{\beta_{01} - \beta_{11}} \approx 208\mu\text{m}$ (highlighted in blue). Since the wavelengths λ_{sw} and λ_{shift1} are nearly the same, this results in a beating of both oscillations, which has practically the same wavelength as the large scale oscillation λ_{shift2} : $\lambda_{\text{beating}} = \frac{\lambda_{\text{sw}}^2}{\lambda_{\text{shift1}} - \lambda_{\text{sw}}} \approx 208\mu\text{m}$.

The whole modulation is therefore periodic with a wavelength of $208\mu\text{m}$, which corresponds to around 390 trapping sites of the standing wave. Assuming that x is the axis of the mode asymmetry, figure 8a) visualizes the resulting pattern for $\xi = 0.2$ and an artificially chosen ratio of $\lambda_{\text{sw}}/\lambda_{\text{shift2}}$, to achieve a meaningful illustration. Obviously, the trapping potential the particle sees is now dependent on the position in axial direction in the fiber. Although the period of the beating pattern is λ_{shift2} , the actual potential shape of the individual trapping positions is periodic in $\frac{\lambda_{\text{shift2}}}{2}$ due to the symmetry of the pattern.

Copropagating LP₁₁ Mode From Both Sides

Analogous to the preceding subsection, we now discuss the effect of two higher order modes propagating in both directions. Assuming that the coupling fraction ξ is equal on both sides, the complex amplitude of the field is given by:

$$\tilde{\mathbf{E}}_{\text{both}}(\mathbf{r}) = \sqrt{P} \left[\varepsilon_{01}(r, \phi) \sqrt{1-\xi} \left(e^{i\beta_{01}z} + e^{-i\beta_{01}z} \right) \right. \\ \left. + \varepsilon_{11}(r, \phi) \sqrt{\xi} \left(e^{i\beta_{11}z} + e^{-i\beta_{11}z} \right) \right] \hat{\mathbf{n}}_{\text{pol}} \quad (27)$$

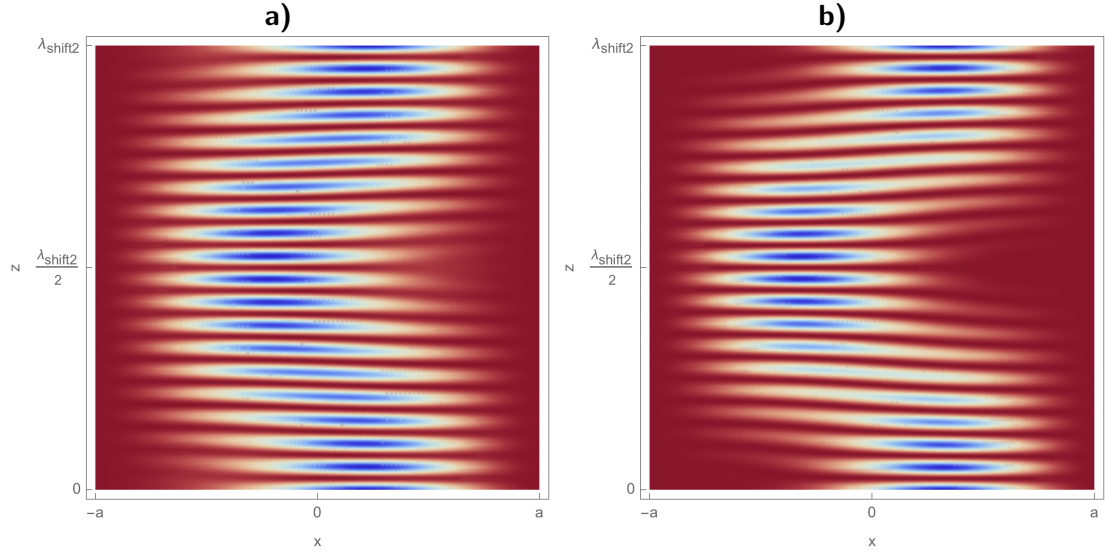


Figure 8: Visualization of the beating pattern formed by a single **a)** and two **b)** additional LP_{11} modes. It is clearly visible, that the main effect is the same in both cases, while two additional modes lead to a more pronounced pattern with stiffer trapping sites. The power in the higher order modes was set to $P\xi$ with $\xi = 0.2$ and an exaggerated ratio of $\lambda_{\text{sw}}/\lambda_{\text{shift}2}$ chosen, in order to arrive at a meaningful illustration. For experimental parameters, the beating periodicity is $\lambda_{\text{shift}2} \approx 208\mu\text{m}$, which corresponds to around 390 trapping positions of the standing wave. It is important to note, that the actual potential shape of the individual trapping positions is periodic in $\frac{\lambda_{\text{shift}2}}{2}$ due to the symmetry of the pattern.

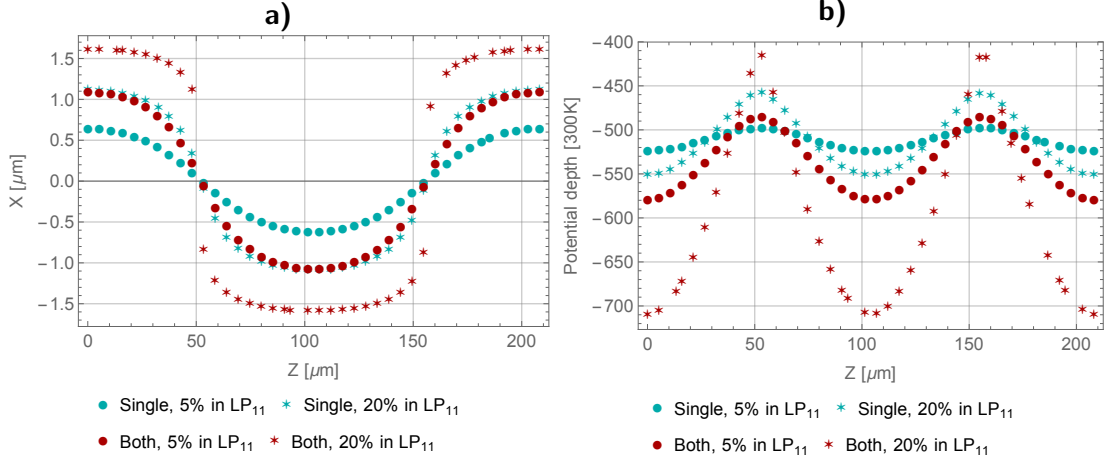


Figure 9: Numerically calculated position of the potential minima **a)** and potential depths **b)** at these minima. The parameters of the calculation are: particle radius $a_p = 150\text{nm}$, total laser power $P = 600\text{mW}$ in both directions, coupling fractions into the higher order mode $\xi = \{0.05, 0.2\}$.

which leads to the optical potential:

$$U_{\text{both}}(\mathbf{r}) = -\text{Re}\{\alpha\}P \left[(1 - \xi)\varepsilon_{01}^2(r, \phi)\cos^2(\beta_{01}z) + \xi\varepsilon_{11}^2(r, \phi)\cos^2(\beta_{11}z) + 2\sqrt{\xi(1 - \xi)}\varepsilon_{01}(r, \phi)\varepsilon_{11}(r, \phi)(\cos((\beta_{01} + \beta_{11})z) + \cos((\beta_{01} - \beta_{11})z)) \right] \quad (28)$$

This expression shows, that the main effect is again a beating pattern with the same periodicities as before. Since the power in the fundamental modes is now smaller in both directions, the effect of the potential shift is greater than in the case of only a one directional higher order mode, which is what one would also intuitively expect. Figure 9 shows numerically calculated potential minima and potential depth for both cases, in steps of roughly ten trapping sites for a whole period of the beating pattern. The calculations were done assuming a particle radius of $a_p = 150\text{nm}$, a total laser power of 600mW in both directions and two coupling fractions into the higher order mode $\xi = \{0.05, 0.2\}$. As we will see in section 4, the particle motion in the trap is a thermally driven harmonic oscillation, with a frequency that depends on the shape and depth of the trapping potential. By measuring this frequency at different positions along the fiber, the varying potential can therefore be experimentally verified.

It needs to be mentioned at this point, that the shown cases of one and two *identical* higher order modes in the fiber only serve as an illustration of the main effects. In the experiment, beating patterns due to higher order modes can occur in various forms, since the asymmetry of the two counter propagating LP_{11} modes will in general not have the same orientation. Due to the degeneracy that was indicated by the index s in subsection 2.3, the axis of asymmetry of the higher order modes can take on any direction in the radial plane, and therefore permits even more complex interference pattern than the ones discussed before.

3. Monitoring the Motion of the Particle

In the last section we learned about the physical mechanism of optical trapping and different geometries in which these traps can occur. The next thing we need for feedback cooling of the particle motion, is a means to detect the trajectory that the particle describes in the trap. The fundamental mechanism behind this relies on the light that is scattered from the particle, and the degree to which this light is coupled into the guiding modes of the HCPCF. It turns out, that the radial position of the particle in the core of the fiber, has a significant influence on whether the light is coupled to asymmetric modes or not. The different guided modes interfere with each other, and thereby imprint information on the particle position on the light that leaves the fiber. A suitable detection scheme is then needed, to extract the information from the emitted light.

3.1. Coupling of the Particle Radiation to the Guiding Modes

As we saw in chapter 2, light in the HCPCF travels in form of the LP guiding modes. The radiation of a trapped particle inside the core of the HCPCF, is partly coupled to the different modes and axially guided to the end of the fiber, and partly escapes the HCPCF through its walls. Since our readout scheme is based on the particle light that is propagated along the fiber in its guiding modes, we first need to quantify the fraction of the power that the different LP modes receive.

For this we use the concept of the mode overlap. Given two light beams described by the electromagnetic fields $\tilde{\mathbf{E}}_{\text{mode}}(\mathbf{r})$ and $\tilde{\mathbf{E}}_{\text{rad}}(\mathbf{r})$, their mode overlap is defined as (Saleh and Teich, 2007):

$$\eta = \frac{\int_A \tilde{\mathbf{E}}_{\text{mode}}^*(\mathbf{r}) \cdot \tilde{\mathbf{E}}_{\text{rad}}(\mathbf{r}) dA}{\sqrt{\int_A |\tilde{\mathbf{E}}_{\text{mode}}(\mathbf{r})|^2 dA \int_A |\tilde{\mathbf{E}}_{\text{rad}}(\mathbf{r})|^2 dA}} \Big|_{z=z_0} \quad (29)$$

where z is assumed as the axis of propagation and the integration is over a plane orthogonal to the z -axis at the point z_0 . The absolute square of η then gives the fraction of the power that is coupled from $\tilde{\mathbf{E}}_{\text{mode}}(\mathbf{r})$ to $\tilde{\mathbf{E}}_{\text{rad}}(\mathbf{r})$.

To treat our specific problem, we consider a particle directly at the entrance of the fiber. Since the numerical aperture of the fiber is very small ($\text{NA} \approx 0.09$), we assume that the amount of light coupled to the guiding modes stays the same, whether the particle is at the entrance or far inside the fiber. As illustrated in figure 10, there are two different kinds of modes describing the propagating light inside and outside of the fiber. In free space, light beams are described by the *Hermite-Gaussian modes* (see appendix A.1.4), which are solutions of the paraxial Helmholtz equation. For a waist of $W_0 = 3.75 \mu\text{m}$ these show a very high mode overlap $|\eta|^2 \simeq 90\%$ with their corresponding LP modes in the fiber. The modes of the whole system, can therefore be described as LP modes inside the HCPCF, which then go over to the corresponding free space modes at the entrance of the fiber.

This allows for a simplification in the calculation of the coupling of the particle radiation to the HCPCF. Since we will see in the next section that it is straightforward

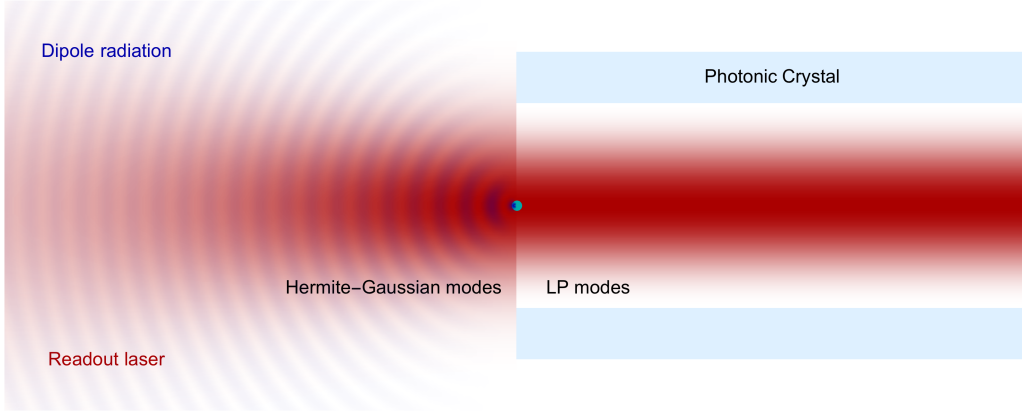


Figure 10: Illustration of the fundamental LP mode propagating in the fiber, its corresponding Hermite-Gaussian mode in free space and the dipole radiation in free space. The mode overlap of the dipole radiation of a particle at the entrance of the fiber with the free space modes, is used to infer its coupling to the corresponding LP modes of the fiber. Although illustrated with two different colors, the readout laser and the induced dipole radiation have the same wavelength.

to find an expression for the particle radiation in free space, we will calculate the mode overlap (29) between the Hermite-Gaussian modes and the particle radiation, to infer the coupling to the corresponding LP modes of the fiber.

3.1.1. Description of the Light Radiated by the Particle

To come up with an expression of the particle radiation, we again approximate the silica bead in the trapping laser as an induced electric dipole. In the upcoming calculations it is enough to work with the expression for the far-field of the radiation. As shown in (Jackson, 1999), this is given by:

$$\tilde{\mathbf{E}}_{\text{dip}}(\mathbf{r}) = \frac{k^2}{4\pi\epsilon_0} \frac{e^{-ikR}}{R} (\hat{\mathbf{r}} \times \mathbf{p}) \times \hat{\mathbf{r}} = \frac{k^2}{4\pi\epsilon_0} \frac{e^{-ikR} \alpha \tilde{\mathbf{E}}_{\text{ind}}(\mathbf{r}_{\text{dip}})}{R} (\hat{\mathbf{r}} \times \hat{\mathbf{n}}_{\text{pol}}) \times \hat{\mathbf{r}} \quad (30)$$

Where \mathbf{r}_{dip} is the position of the dipole, R is the distance from the dipole to the point where the field is evaluated, $\tilde{\mathbf{E}}_{\text{ind}}$ the complex amplitude of the inducing field, $\hat{\mathbf{n}}_{\text{pol}}$ its polarization vector and α the polarizability of the particle, given by (11). In the case of an inducing field that is polarized in z direction, the angular distribution of the radiated power is given by:

$$\frac{dP_{\text{dip}}}{d\Omega} = \frac{c\pi^2}{2\epsilon_0\lambda^4} |\alpha|^2 |\tilde{\mathbf{E}}_{\text{ind}}(\mathbf{r}_{\text{dip}})|^2 \sin^2(\vartheta) \quad \left[\frac{dP_{\text{dip}}}{d\Omega} \right]_{\text{norm}} = \frac{3}{8\pi} \sin^2(\vartheta) \quad (31)$$

Here, ϑ is the polar angle. The second equation on the right hand side gives the normalized angular distribution of the power, which we will need for the calculation of the mode overlap. The total average power radiated by the dipole is given by:

$$\langle P_{\text{dip}} \rangle = \frac{4c\pi^3}{3\epsilon_0\lambda^4} |\alpha|^2 |\tilde{\mathbf{E}}_{\text{ind}}(\mathbf{r}_{\text{dip}})|^2 \quad (32)$$

Simplification and Normalization of the Dipole Radiation

The Hermite-Gaussian beams are solutions of the paraxial Helmholtz equation. For the purpose of calculating the mode overlap with the dipole radiation, we can also treat the dipole radiation in the paraxial approximation $z \gg r = \sqrt{x^2 + y^2}$, where z is the axis of the fiber core, which demands that the polarization of the inducing field $\hat{\mathbf{n}}_{\text{pol}}$ lies in the x - y plane. This allows for great simplifications in expression (30). Using $R \simeq z$ and neglecting all terms of the form $\frac{r}{z}$, the double cross product can then be approximated as:

$$(\hat{\mathbf{r}} \times \hat{\mathbf{n}}_{\text{pol}}) \times \hat{\mathbf{r}} \simeq \hat{\mathbf{n}}_{\text{pol}}$$

In the exponent of the phase term, we include the first higher order term in the approximation of R , which is the common procedure (Saleh and Teich, 2007):

$$R = \sqrt{z^2 + r^2} = z \sqrt{1 + \left(\frac{r}{z}\right)^2} = z \left(1 + \frac{1}{2} \left(\frac{r}{z}\right)^2 + \mathcal{O}\left[\left(\frac{r}{z}\right)^4\right]\right) \stackrel{r \ll z}{\simeq} z + \frac{x^2 + y^2}{2z}$$

Summarizing, this allows us to write the dipole radiation as:

$$\tilde{\mathbf{E}}_{\text{dip}}(\mathbf{r}) = \frac{k^2 \alpha \tilde{E}_{\text{ind}}(\mathbf{r}_{\text{dip}})}{4\pi\epsilon_0} \frac{1}{z} e^{-ik\left(z + \frac{x^2 + y^2}{z}\right)} \hat{\mathbf{n}}_{\text{pol}} \quad (33)$$

For the calculation of the mode overlap, we need the normalized expressions of the fields. We achieve this by demanding, that the angular distribution of the absolute square of (33) in a small cone around the z -axis, is equal to the normalized expression in (31):

$$\tilde{\mathbf{A}}_{\text{dip}}(\mathbf{r}) = \frac{1}{2} \sqrt{\frac{3}{2\pi}} \frac{1}{z} e^{-ik\left(z + \frac{x^2 + y^2}{z}\right)} \hat{\mathbf{n}}_{\text{pol}} \quad (34)$$

This is also known as a paraboloidal wave and, like the Hermite-Gaussian beams, a solution of the paraxial Helmholtz equation.

3.1.2. Calculation of the Mode Overlap

To quantify the coupling of the particle radiation to the guiding modes, we will now calculate the mode overlap of the particle radiation described by (34), with the normalized Hermite-Gaussian modes. The latter are given in appendix A.1.4. As we will see in the upcoming section 3.2, the detection schemes of the particle motion only make use of the fundamental and the first higher order mode, while suppressing any other incoming modes. We can therefore restrict our calculations in this section to these two. For this,

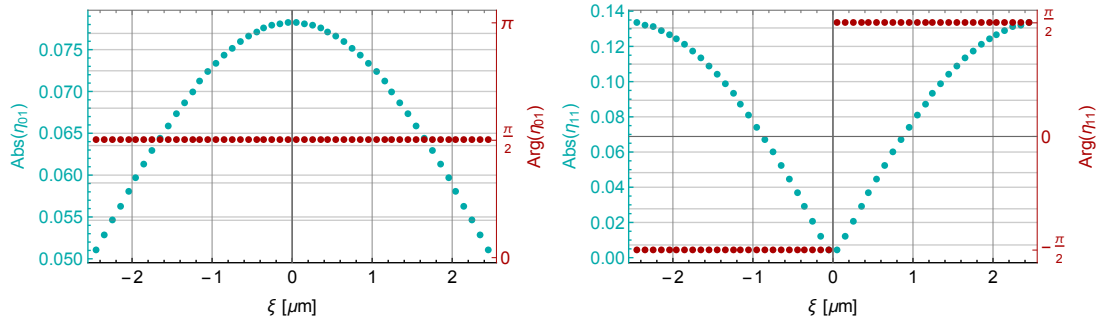


Figure 11: Numerically calculated values of the mode overlaps, for different displacements ξ of the particle. The values of the coupling constants are purely imaginary, reflecting a phase shift of the coupled light by $\frac{\pi}{2}$ or $-\frac{\pi}{2}$, with respect to the readout laser. The linear behavior of η_{11} at the center of the core, will be of importance for the signal size of the radial detection scheme.

we set the entrance of the fiber to be at $z = 0$ and the center of the core at $x = y = 0$. To describe the workings of our optical readout, we are not only interested in the size of the coupling, but also in how it changes for displacements of the particle from the middle of the fiber. Without loss of generality, we set this to be in x direction and denote the size of the shift with ξ . For reasons of symmetry, it is then sufficient to calculate the mode overlap with the fundamental and the first higher order mode whose axis of asymmetry lies in x . We explicitly state the expressions for these two:

$$\eta_{01}(\xi) = \frac{\sqrt{3}}{2\pi} \frac{1}{W(z)z} \int_{\mathbb{R}^2} e^{-\frac{x^2+y^2}{W^2(z)}} e^{-i\left(k\left(\frac{x^2+y^2}{2R(z)} - \frac{(x-\xi)^2+y^2}{2z}\right) - \zeta(z)\right)} dx dy \Bigg|_{z=z_0} \quad (35)$$

$$\eta_{11}(\xi) = \sqrt{\frac{3}{2}} \frac{1}{\pi W(z)z} \int_{\mathbb{R}^2} x e^{-\frac{x^2+y^2}{W^2(z)}} e^{-i\left(k\left(\frac{x^2+y^2}{2R(z)} - \frac{(x-\xi)^2+y^2}{2z}\right) - 2\zeta(z)\right)} dx dy \Bigg|_{z=z_0} \quad (36)$$

Where z_0 denotes the plane in which the overlap is evaluated and we stick to the index convention of the LP modes for the labeling of the mode overlaps. In the far field where z is large compared to the Rayleigh length $z_R = \frac{\pi W_0^2}{\lambda}$ of the Hermite-Gaussian beams, this integral converges to a definite value for displacements of the particle ξ that are small with respect to W_0 . Figure 11 shows numerical results on the coupling constant η , evaluated at a distance $z_0 = 10^6 z_R$ from the particle. As we can see, the coupling constant is purely imaginary, which reflects a phase shift to the coupled light by either $\frac{\pi}{2}$ or $-\frac{\pi}{2}$, relative to the readout laser. Reflecting the shape of the Hermite-Gaussian modes, $\Im\{\eta_{01}\}$ is symmetric, and $\Im\{\eta_{11}\}$ antisymmetric with respect to the center of the core. As we will see in the upcoming section, the signal size of the radial readout depends on the change of the coupling strength, for small movements of the particle. It is therefore important to note the linear behavior of $\eta_{11}(\xi)$ at the center of the core.

3.2. Detection of the Particle Motion

The information on the particle position is stored in the interference pattern of the different modes, to which the particle radiation is coupled. In order to extract this information, a special detection scheme is needed. While we will see that for the detection of the axial motion, a single photodetector to measure the total laser power leaving the fiber is sufficient, the radial readout turns out to be more elaborate. As already done by (Gieseler et al., 2012; Li et al., 2011), we implement a so called *balanced detection*. The principle idea is, that the motion of the particle causes a spatial asymmetry of the beam, in the direction of the particle motion. By cutting the beam in to halves and measuring their powers separately, one can then quantify this asymmetry as difference in power and use it as an indicator of the radial particle position. This is done separately for the two orthogonal radial directions.

In the following mathematical treatment, we will consider only the field at the end of the fiber, as described by the LP modes. This is possible, since the optical elements that follow, merely image the end of the fiber to the detection scheme (Kogelnik and Li, 1966), and do not change the spatial symmetries of the beam. This can intuitively be understood, since for all LP modes relevant for the readout, there is a corresponding Hermite-Gaussian mode of free space propagation, that resembles its shape (see appendix A.1.4).

3.2.1. Detection of the Radial Motion

Let us assume, that the particle is trapped at a distance x_{tr} from the center of the core and consider only the motion of the particle in direction of the x -axis. Detecting the movement in y direction works analogously. Around the trapping site, the particle then performs a motion described by x_{p} . The distance of the particle from the core center is therefore $x = x_{\text{tr}} + x_{\text{p}}$. For reasons already explained in section 1.2, we use a separate laser with a wavelength of $\simeq 1100\text{nm}$ for the radial readout of the particle motion, which is coupled into the fiber from the right side⁵. Using the notation of subsection 2.6, the complex amplitude of the electric field is then given by:

$$\begin{aligned} \tilde{\mathbf{E}}_{\text{det}}(\mathbf{r}) = & \left(\sqrt{P_{\text{rl}}}\varepsilon_{01}(r, \phi)e^{i\beta_{01}z} \right. \\ & \left. + \eta_{01}(x)\sqrt{P_{\text{dip}}(x)}\varepsilon_{01}(r, \phi)e^{i\beta_{01}z} + \eta_{11}(x)\sqrt{P_{\text{dip}}(x)}\varepsilon_{11}(r, \phi)e^{i\beta_{11}z} \right) \mathbf{n}_{\text{pol}} \end{aligned} \quad (37)$$

Where the first term stems from the readout laser itself, with P_{rl} being its total power, and the other two describe the light from the particle, that is traveling in the modes along the fiber. P_{dip} is the power radiated from a particle at x into the coupling cone of the fiber, in the direction of the detection setup. The x dependence of P_{dip} stems from the inducing field, as can be seen in equation (32). Since we only consider oscillations around the trapping site, expressed by $x = x_{\text{tr}} + x_{\text{p}}$, and these are much smaller than

⁵The field that induces the relevant particle radiation is therefore given by a single LP₀₁ mode, propagating in one direction, and not a standing wave as in the case of the trapping laser.

the FWHM of the field, it is justified to replace $P_{\text{dip}}(x)$ with $P_{\text{dip}}(x_{\text{tr}})$. From this we can calculate the intensity of the field:

$$\begin{aligned}
I_{\text{det}}(r, \phi) &= \frac{1}{2} \epsilon_0 c |\tilde{\mathbf{E}}_{\text{det}}(\mathbf{r})|^2 \\
&= \frac{1}{2} \epsilon_0 c ((P + P_{\text{dip}}(x_{\text{tr}}) \eta_{01}(x)) \varepsilon_{01}^2(r, \phi) + P_{\text{dip}}(x_{\text{tr}}) \eta_{11}(x) \varepsilon_{11}^2(r, \phi) \\
&\quad + 2\sqrt{PP_{\text{dip}}(x_{\text{tr}})} |\eta_{01}(x)| \varepsilon_{01}^2(r, \phi) \cos(\phi_{01}(x)) \\
&\quad + 2\sqrt{PP_{\text{dip}}(x_{\text{tr}})} |\eta_{11}(x)| \varepsilon_{01}(r, \phi) \varepsilon_{11}(r, \phi) \cos(z(\beta_{01} - \beta_{11}) - \phi_{11}(x)) \\
&\quad + 2P_{\text{dip}}(x_{\text{tr}}) |\eta_{01}(x)| |\eta_{11}(x)| \varepsilon_{01}(r, \phi) \varepsilon_{11}(r, \phi) \cos(z(\beta_{01} - \beta_{11}) - \phi_{11}(x)))
\end{aligned} \tag{38}$$

Where we write the coupling constants as $\eta_{nm}(x) = |\eta_{nm}(\rho)| e^{i\phi_{nm}(x)}$. Since $P_{\text{dip}} \ll P$, all terms that have a linear dependence on P_{dip} can be neglected (illustrated with grey color). After this reduction, there are two x dependent terms remaining. One of them is spatially symmetric and the other antisymmetric, as can be seen from the spatial functions $\varepsilon_{01}(r, \phi)$ and $\varepsilon_{11}(r, \phi)$. As we saw in figure 11, which illustrates the coupling strength of the particle radiation to the LP modes, the coupling to the LP₁₁ mode is linear for the great part of the fiber core. Since it is the change in the position, that we are interested in, the linear coupling will provide the biggest signal strength. Therefore we must find a way, to extract only the term involving the coupling constant $\eta_{11}(x)$ (illustrated in red color).

For this we will exploit the fact, that the term we are interested in is spatially antisymmetric. Figure 12 illustrates the main idea behind the detection scheme. The beam is cut in to equal halves, which are then sent to a photodetector and the total power in each half separately detected. The two signals are then subtracted from each other, which gives a signal that is proportional to the radial particle displacement in the direction in which the beam is cut, and strongly suppresses (around three orders of magnitude) the symmetric parts of the beam. Mathematically, this corresponds to a separate integration over the two spatial halves of expression (38), and a subtraction of them from each other. This eliminates all but the antisymmetric term⁶, and the particle position signal is then given by:

$$\begin{aligned}
P_{\text{diff}}(x) &= 4\tau \sqrt{PP_{\text{dip}}(x_{\text{tr}})} |\eta_{11}(x)| \cos(z(\beta_{01} - \beta_{11}) - \phi_{11}(x)) \\
&= 8\tau \sqrt{P \frac{c\pi^3}{3\epsilon_0 \lambda^4}} |\alpha| |\tilde{\mathbf{E}}_{\text{ind}}(x_{\text{tr}})| |\eta_{11}(x)| \cos(z(\beta_{01} - \beta_{11}) - \phi_{11}(x))
\end{aligned} \tag{39}$$

Where we defined the constant $\tau = \frac{1}{2} \epsilon_0 c \int_{A/2} \varepsilon_{01}(r, \phi) \varepsilon_{11}(r, \phi) dA \approx 0.4$. In line two we substituted for the total power radiated by the dipole (eq. (32)).

Under general circumstances, the readout strength also depends on the field of the readout laser at the trapping positions, since it affects the power that is reradiated by

⁶In experimental settings this has the benefit of suppressing any existing intensity noise in the symmetric parts of the trapping beams.

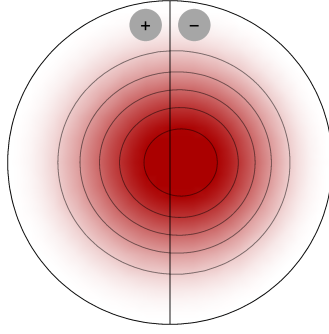


Figure 12: Exaggerated illustration of the radial detection. The beam leaving the HCPCF has a small asymmetry in the power distribution due to the displacement of the particle, and is cut in two equal halves. The power in both halves is then detected with photodetectors. The two signals are then subtracted from each other, giving a signal that is proportional to the radial displacement of the particle.

the particle. In the discussion of copropagating higher order modes of subsection 2.6 we saw, that this can take on complex forms, and would therefore lead to additional complexity. In order to focus on the readout itself though, without making detailed assumptions on the field of the inducing beam, we will therefore simplify the treatment by choosing the field at the trapping position to be equal to the center of a LP_{01} mode. The final expression for the power difference at the detector is then given by:

$$P_{\text{diff}}(x) = \sqrt{\frac{2\pi^3}{3}} \frac{8\tau P}{\epsilon_0 \lambda^2} \zeta_{01} |\alpha| |\eta_{11}(x)| \cos(z(\beta_{01} - \beta_{11}) - \phi_{11}(x)) \quad (40)$$

It is important to note, that this expression also depends on the axial position of the particle, and that the readout sensitivity shows the same periodic behavior as the trapping potential in subsection 2.6. Furthermore, by dividing it by P , we get an expression for the ratio of the power difference to the total power of the readout beam. Since this stays constant during the propagation of the readout beam to the equipment of the balanced detection, we can use it to calculate the actual signal size at the detector from the beam power P_{det} on the diodes of the detector.

Signal Size of the Particle Oscillation

As a last thing in this subsection, we calculate numerical values for the size of the voltage signal at the detector, corresponding to the particle movement in the optical potential. In section 4 this will be shown to have an average amplitude around 50nm. The detector we use in the experiment has a conversion gain for the detected power difference of $2.5 \times 10^5 \text{V/W}$, and using expression (40) we can now easily calculate the signal size of a particle oscillation around several trapping positions x_{tr} .

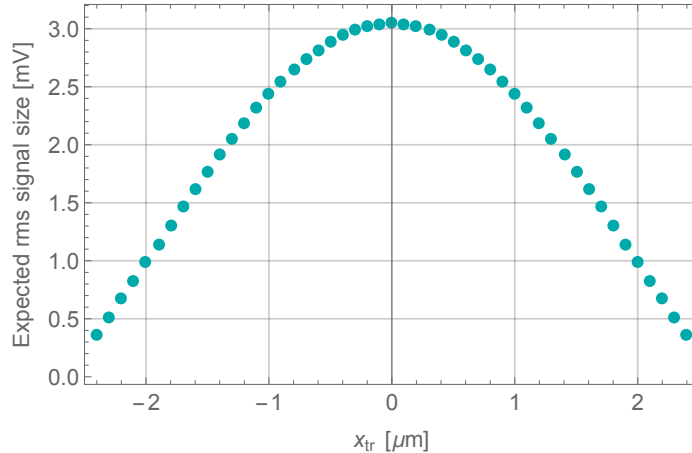


Figure 13: Root mean square size of the voltage signal, expected at the output of the detector for a total incoming power of $P_{\text{det}} = 0.1\text{mW}$ on the diodes, a particle radius of $a_{\text{particle}} = 150\text{nm}$, laser wavelength of $\lambda = 1100\text{nm}$ and amplitude of the particle oscillation of 50nm . It is emphasized, that the x -axis of the graph shows the trapping position of the particle, where it performs the oscillation.

Figure 13 shows the result of such a calculation for typical experimentally parameters of $\lambda = 1100\text{nm}$, $P_{\text{det}} = 0.1\text{mW}$, $a_p = 150\text{nm}$ and an oscillation amplitude of 50nm . The axial position was set to $z = 0$ in order to get the biggest possible signal. Comparing this with the results of subsection 2.6, we expect at least a signal with a root mean square size of 0.5mV , which will become important in the discussion of the experimental results.

3.2.2. Detection of the Axial Motion

Although the focus of the experiment is feedback cooling of the radial motion, detection of the axial motion is useful to get additional information on the particle. Unlike the balanced detection, it is based only on the fundamental guiding mode. The basic principle builds on the interference of the light scattered by the particle from the clockwise propagating beam, with the transmitted counter-clockwise propagating beam. As illustrated in figure 14, the light that falls on the detector comes from the counter-clockwise propagating beam, and the radiation of the particle. The latter one though, is induced by both trapping beams and therefore includes either their phases. If the particle changes its position in axial direction, the path length of one beam gets shorter and the other longer, resulting in a changed relative phase. We restrict the mathematical treatment to the case of a particle that is only moving in axial direction, which is a good approximation due to the small amplitude of the radial motion. The complex amplitude of the electric field that the particle then sees at the trapping position, which we define to be

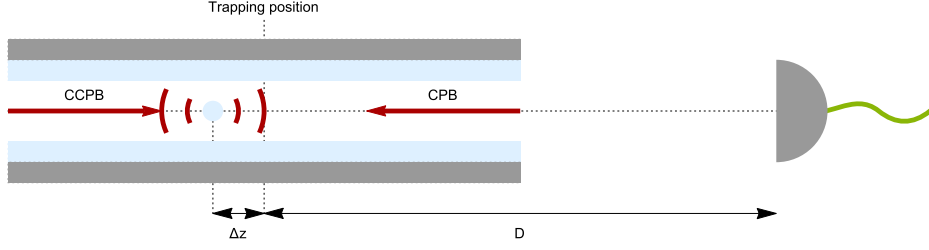


Figure 14: Illustration of the parameters which are important for the detection of the axial particle motion. Δz denotes the distance in axial direction of the particle from the trapping position, and D is the distance from the trapping position to the photodetector. For the mathematical treatment, we assume that the particle is only moving in axial direction.

at $z = 0$, is then given by⁷:

$$\tilde{\mathbf{E}}_{\text{sw}}(r, \phi, z = 0) = \sqrt{P}\varepsilon_{01}(r, \phi) \left(e^{i\vartheta_{\text{cpb}}} + e^{i\vartheta_{\text{ccpb}}} \right)$$

Where we defined ϑ_{cpb} and ϑ_{ccpb} as the phases of the trapping beams at $z = 0$. In the case of a standing wave trap, the trapping positions are exactly at those points, where the phases of cpb and ccpb are equal up to multiples of 2π . Therefore, we can neglect them as a global phase. On the other hand, since the beams travel in opposite directions, a small axial displacement Δz of the particle, introduces a relative phase:

$$\tilde{\mathbf{E}}_{\text{sw}}(r, \phi, \Delta z) = \sqrt{P}\varepsilon_{01}(r, \phi) \left(e^{-i\beta_{01}\Delta z} + e^{i\beta_{01}\Delta z} \right)$$

This field then induces the radiation of the particle, which is coupled to the LP_{01} mode of the fiber, and propagates to the detector along with the clockwise propagating beam. The propagation to the detector results only in an additional global phase, which is not relevant for the detection, and is therefore neglected. Using the same notation as in the last section, the electric field at the detector is then given by:

$$\begin{aligned} \tilde{\mathbf{E}}_{\text{det}}(r, \phi, z) &= \sqrt{P}\varepsilon_{01}(r, \phi) \\ &+ \sqrt{P_{\text{dip}}}\varepsilon_{01}(r, \phi)|\eta_{01}(r)|e^{i\phi_{01}(r)} \left(1 + e^{2i\beta_{01}\Delta z} \right) \end{aligned} \quad (41)$$

The detector gives out a signal that is proportional to the integrated intensity of this field, where the latter can be calculated to be:

$$\begin{aligned} V_{\text{det}}(\Delta z) &\propto \int_A I_{\text{det}}(r, \phi, \Delta z) dA \\ &= P + 4P_{\text{dip}}|\eta_{01}(r)|^2 \cos^2(\beta_{01}\Delta z) \\ &\quad + 2\sqrt{PP_{\text{dip}}}\eta_{01}(r) (\cos(\phi_{01}(r)) + \cos(2\beta_{01}\Delta z + \phi_{01}(r))) \end{aligned} \quad (42)$$

⁷We again use the notation for the LP modes, that was introduced in section 2.6.

Again A denotes the area of the whole beam. Since $P \gg P_{\text{dip}}$, the only relevant Δz dependent term is the last one marked in red. From the calculations on the mode overlap we know, that it $\phi_{01}(r) = \frac{\pi}{2}$ for the relevant radial displacements. The relevant term for the axial readout therefore becomes:

$$V_{\text{det}}(\Delta z) \propto P + 4P_{\text{dip}}|\eta_{01}(r)|^2 \cos^2(\beta_{01}\Delta z) - 2\sqrt{PP_{\text{dip}}}\eta_{01}(r) \sin(2\beta_{01}\Delta z) \quad (43)$$

4. Center of Mass Motion, Parametric Feedback and Experimental Results

The goal of the experiment described in this thesis, is to cool the center of mass motion that the particle describes in the optical potential. The theoretical description of this, and the experimental measured data on the readout as well as the feedback cooling, are the main topic of this section. For the sake of a complete understanding, we will start with a theoretical description of the particle motion itself, which will lead us to the discussion of the so called *Brownian motion*. It then turns out, that in the case of a trapped particle, its motion is that of a damped and thermally driven harmonic oscillator. By comparing the theoretically expected behavior of the particle with experimentally measured data from the axial and radial readouts, we then verify the validity of the description and confirm that the readouts are working properly. The final part of the section is the discussion of the feedback cooling mechanism, its influence on the particle motion and a discussion of the experimental results.

4.1. Brownian Motion of a Free Particle

If a particle that is suspended in a liquid or air, moves under the influence of the particles that constitute the surrounding medium, the trajectory that it describes is denoted as Brownian motion. In this case, the dynamics for the translational degrees of freedom are given by a *Langevin equation*, which for a free particle in cartesian coordinates (here shown in the case of the x-axis) takes on the form (Li, 2011; Uhlenbeck and Ornstein, 1930):

$$M \frac{d^2x}{dt^2} + \gamma \frac{dx}{dt} = F_{\text{therm}}(t) \quad (44)$$

Where x denotes the center of mass position on the x-axis, M is the mass itself and $F_{\text{therm}}(t) = \sqrt{2k_B T \gamma} \zeta(t)$ the stochastic force that the particle experiences due to the interaction with the surrounding medium. In there, $\zeta(t)$ is a normalized white noise process, which therefore fulfills the relations:

$$\langle \zeta(t) \rangle = 0 \quad \langle \zeta(t) \zeta(t') \rangle = \delta(t - t')$$

Where the brackets denote the average over an ensemble of identically prepared particles. It is important to note, that the damping factor γ occurs in the friction term $\gamma \dot{x}$ as well as in the stochastic force. This reflects the fact that it is the surrounding medium, that both drives the motion of the particle and damps any already existing movement. By solving the stochastic differential equation (44) and using the relations for $\zeta(t)$, one can derive the mean square displacement of the particle motion:

$$\langle (x(t) - x(0))^2 \rangle = \langle |\Delta x(t)|^2 \rangle = \frac{2k_B T}{M \Gamma_0^2} (\Gamma_0 t - 1 + e^{-\Gamma_0 t}) \quad (45)$$

Where k_B is Boltzmanns constant and we defined $\Gamma_0 = \frac{\gamma}{M} = \frac{1}{\tau_p}$, with τ_p being the relaxation time of the particle momentum. Looking at equation (45) we can distinguish

the following two regimes:

$$\langle |\Delta x^i(t)|^2 \rangle = \begin{cases} \frac{k_B T}{M} t^2 & t \ll \tau_p \\ \frac{2k_B T}{M\Gamma_0} t = 2Dt & t \gg \tau_p \end{cases}$$

Where $D = \frac{k_B T}{M\Gamma_0}$ is the diffusion constant derived by Albert Einstein in 1905 (Einstein, 1905). This shows that the particle behaves ballistically on a small timescale, while exhibiting diffusive motion on longer timescales.

4.1.1. Pressure Dependence of the Damping

In the experiment, the surrounding medium is always air at various pressures. The latter influences the motion of the particle via the damping constant Γ_0 , which is given by (Beresnev et al., 2006; Li et al., 2011; Gieseler et al., 2012):

$$\Gamma_0 = \frac{6\pi\eta r}{m} \frac{0.619}{0.619 + \text{Kn}} (1 + c_K) \quad \text{with} \quad c_K = \frac{0.31\text{Kn}}{0.785 + 1.152\text{Kn} + \text{Kn}^2} \quad (46)$$

Where Kn is the Knudsen number given by $\text{Kn} = \frac{l_{\text{fp}}}{a_{\text{part}}}$, in which l_{fp} is the mean free path and is itself given by $l_{\text{fp}} = \frac{k_B T}{\pi\sqrt{2}\sigma p}$. Here p is the pressure of the air and σ denotes the mean cross section of the air molecules. In calculations we will use $\sigma = 0.37\text{nm}$. Figure 15a) illustrates the pressure dependence of the friction coefficient Γ_0 for a particle with a radius of 150nm.

4.2. Brownian Motion of a Particle in an Optical Potential

A particle in equilibrium with its surrounding medium at room temperature, will only perform small oscillations in a potential with a depth of $\simeq 500k_B T_{\text{room}}$ as shown in fig. 6 for the standing wave case. Under these circumstances, we can approximate the potential around the trapping site by a harmonic potential, described by the spring constant κ . The Langevin equation describing the dynamics of the particle is then the differential equation of a stochastically driven, damped harmonic oscillator:

$$\frac{d^2 x}{dt^2} + \Gamma_0 \frac{dx}{dt} + \Omega_0^2 x = \sqrt{\frac{2k_B T \Gamma_0}{M}} \zeta(t) \quad (47)$$

With $\Omega_0 = \sqrt{\frac{\kappa}{M}}$ being the frequency of the undamped oscillator, while the frequency of the damped oscillator is given by $\Omega_D = \sqrt{\Omega_0^2 - \Gamma_0^2/4}$. As usual in the treatment of the damped harmonic oscillator, we therefore distinguish between the overdamped $\frac{2\Omega_0}{\Gamma_0} < 1$, critically damped $\frac{2\Omega_0}{\Gamma_0} = 1$ and underdamped $\frac{2\Omega_0}{\Gamma_0} > 1$ regime. Another very important quantity is the so called quality factor of an oscillator, which is given by the ratio of frequency to damping rate $Q := \frac{\Omega_0}{\Gamma_0} = \tau_p \Omega_0$, and can be understood as the average number of full oscillations, that the particle performs before it interacts with the surrounding medium.

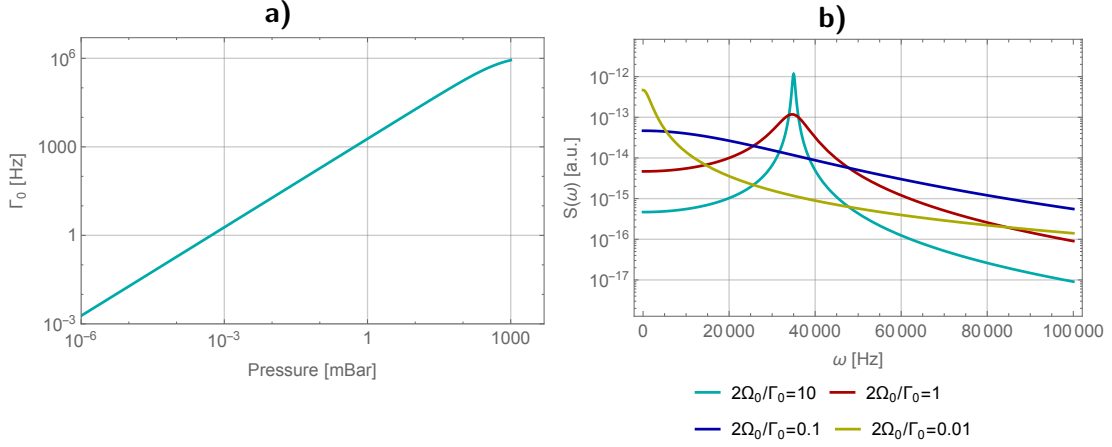


Figure 15: **a)** Calculated pressure dependence of the friction coefficient Γ_0 for a particle with a radius of 150nm. **b)** Power spectral density for different frictional coefficients of a particle in a potential with frequency $\Omega_0 = 35\text{kHz}$, that is comparable to the radial potential in the experiment.

4.2.1. Powerspectrum of a Trapped Particle

A lot of information on the particle motion can be gained by looking at the power spectrum of the motion, which is calculated from the squared modulus of the fourier transform (Li, 2011):

$$\tilde{x}_k = \int_{-\frac{T_{\text{rec}}}{2}}^{\frac{T_{\text{rec}}}{2}} e^{i\omega_k t} x(t) dt \quad (48)$$

and analogously for $\tilde{\zeta}_k$. Here T_{rec} is the length of the experimentally recorded time trace $x(t)$ of the particle and the frequency is given by $\omega_k = \frac{2\pi k}{T_{\text{rec}}}$. Applying this to equation (54) we end up with:

$$-\omega_k^2 \tilde{x}_k - i\omega_k \Gamma_0 \tilde{x}_k + \Omega_0^2 \tilde{x}_k = \xi \tilde{\zeta}_k \quad \Rightarrow \quad \tilde{x}_k = \frac{\xi \tilde{\zeta}_k}{\Omega_0^2 - \omega_k^2 - i\omega_k \Gamma_0}$$

The power spectral density of a particle time trace is then defined as:

$$S_k \equiv \frac{|\tilde{x}_k|^2}{T_{\text{rec}}} = \frac{|\tilde{\zeta}_k|^2}{T_{\text{rec}}} \frac{2k_B T}{M} \frac{\Gamma_0}{(\Omega_0^2 - \omega_k^2)^2 + \omega_k^2 \Gamma_0^2}$$

From the properties of the stochastic force one can easily derive the relation $\langle \tilde{\zeta}_k \tilde{\zeta}_l \rangle = T_{\text{rec}} \delta_{kl}$. Using this, one can state the form of the averaged power spectral density, which in theory for an infinitely long trimetrace becomes:

$$S(\omega) \equiv \langle S_k \rangle = \frac{2k_B T}{M} \frac{\Gamma_0}{(\Omega_0^2 - \omega^2)^2 + \omega^2 \Gamma_0^2} \quad (49)$$

Figure 15b) shows the power spectral density of a particle with radius 150nm in a potential with a frequency of $\Omega_0 = 35\text{kHz}$, which is comparable to the radial potential in the experiment. By calculating the power spectral density of an experimentally recorded time trace of the particle motion, and fitting it with the theoretical shape given in (49), we therefore can get information on the frequency of the potential, the frictional coefficient Γ_0 and the temperature T of the medium surrounding the particle.

Before we close this subsection, we give a very important relation which can be derived by using Parseval's theorem, and connects the mean square displacement of the particle, with the area under the curve of the power spectral density and the temperature of the surrounding medium:

$$\langle x^2 \rangle = \frac{1}{\pi} \int_0^{\infty} S(\omega) d\omega = \frac{k_B T}{M \Omega_0^2} \quad (50)$$

Which one could also derive for an undamped harmonic oscillator, using the equipartition theorem.

4.3. Calculation of the Trap Frequencies

We will now calculate the expected frequencies of the trapping potentials discussed in section 2. As already mentioned in the last subsection, we therefore approximate the trap by a harmonic potential. This we can do, by calculating the Taylor series of the potential around the trapping position x_{tr} , neglecting everything after the quadratic term:

$$U_{\text{pot}}(x) \simeq \underbrace{U(x_{\text{tr}})}_{=: U_0} + \underbrace{U'(x_{\text{tr}})}_{=0} (x - x_{\text{tr}}) + \frac{1}{2} U''(x_{\text{tr}}) (x - x_{\text{tr}})^2 \quad (51)$$

Where the first derivative vanishes, since the trapping position is at a minimum of the potential. Comparing this with the general expression for the potential of a harmonic oscillator $U_{\text{harm}}(x) = U_0 + \frac{M \Omega_0^2 x^2}{2}$, we arrive at an expression for the frequency of the potential:

$$\Omega_0 = \sqrt{\frac{U''(x_{\text{tr}})}{M}} \quad (52)$$

Frequencies of the Standing Wave Potential

We now want to give expressions for the main trapping potential by the standing wave of the LP_{01} modes. This was discussed in section 2.5 and the expression for the potential can be found in equation (19). The trapping position for this configuration is simply $r = 0$ and $z = 0$. A straightforward calculation and using equation (52) gives:

$$\Omega_{\text{radial}} = \frac{u_{01}}{a_c^2 J_1(u_{01})} \sqrt{\frac{2 \text{PRe}\{\alpha\}}{\pi c \epsilon_0 M}} \quad \Omega_{\text{axial}} = \frac{2 \beta_{01}}{a_c J_1(u_{01})} \sqrt{\frac{\text{PRe}\{\alpha\}}{\pi c \epsilon_0 M}}$$

Which can be simplified with the approximation of $\text{Re}\{\alpha\}$ given in (12), and by writing the mass of the particle as $M = \frac{4\pi a_p^3 \rho}{3}$, where ρ is the mass density of silica:

$$\Omega_{\text{radial}} = \frac{u_{01}}{a_c^2 J_1(u_{01})} \sqrt{\frac{6P}{\pi c \rho} \left(\frac{\epsilon - 1}{\epsilon + 2} \right)} \quad \Omega_{\text{axial}} = \frac{2\beta_{01}}{a_c J_1(u_{01})} \sqrt{\frac{3P}{\pi c \rho} \left(\frac{\epsilon - 1}{\epsilon + 2} \right)} \quad (53)$$

For experimental parameters, this shows that the axial frequency is bigger than the radial by a factor of $\frac{\Omega_{\text{axial}}}{\Omega_{\text{radial}}} = \frac{\sqrt{2} a_c \beta_{01}}{u_{01}} \approx 17$, which is what we intuitively expected from the trapping geometry. The numerical values for the frequencies in the case of a trapping power of 600mW are $\Omega_{\text{radial}} \approx 18\text{kHz}$ and $\Omega_{\text{axial}} \approx 315\text{kHz}$. It is interesting to note, that in the approximated form which is valid for $a_p \ll \lambda$, the frequencies do not depend on the actual size of the particles, but only on the density ρ of the material they are made from.

Modulation of the Frequencies in the Case of Copropagating Higher Order Modes

As we have seen in subsection 2.6, a trap formed by LP_{01} and LP_{11} modes exhibits a periodic modulation of the trapping potential, which periodically shifts the trapping sites from the center of the core into the direction of asymmetry of the LP_{11} mode. We now numerically investigate the effect that this has on the frequencies of resulting traps, and their dependence on the axial position in the fiber. Figure 16 shows the numerically calculated trap frequencies for the same configuration as in subsection 2.6, which is a trapping beam power of 600mW and a particle with a radius of $a_p = 150\text{nm}$. The direction of the LP_{11} mode asymmetry is again x .

As we can see, the frequency shows the same periodic behavior as the trapping potential. The size of the modulation depends on the fraction of the trapping beam power, that is propagating in the higher order modes, and is stronger in the direction of asymmetry. In the following subsection we will discuss experimental results on this effect.

4.4. Experimental Timetraces and Power Density Spectra

In this section we discuss experimental results on the particle motion detection. We use the optical readout to record time traces of the particle motion, which are then analyzed in post processing. Doing this for different pressures, trapping positions and powers, allows us to characterize the optical trap and compare the observed physical dynamics with the theoretical predictions.

4.4.1. Typical Example of Readout Data

Figure 17 shows parts of three typical time traces, taken from a particle at a pressure of $(4.2 \pm 1.3)\text{mBar}$ and a trapping beam power of 600mW. In order to make the motion of the particle visible, the time traces were filtered in post processing, using a digital bandpass filter from 20-60kHz in radial, and from 480-560kHz in axial direction. The size of the signal was found to be in the mV regime, as expected from the theoretical estimation (see figure 13).

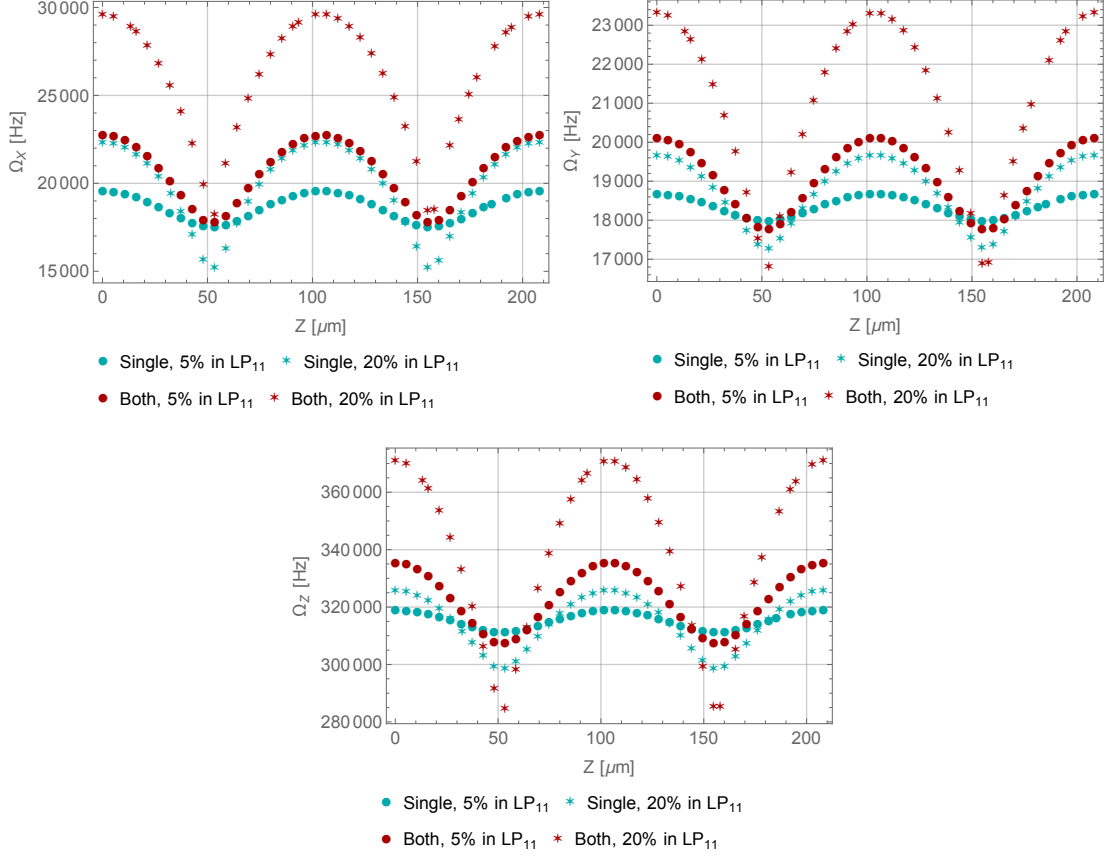


Figure 16: Numerically calculated trap frequencies for the same configurations as in subsection 2.6. The upper two plots show the radial, and the lower one the axial direction. Cyan colored points show the scenario of a single LP_{11} mode, coupled into the fiber from one side and red points correspond to the case of a coupling from both sides. The calculation was done for a coupling of 5% and 20% into the LP_{11} modes. As in section 2.6, the direction of mode asymmetry is x . This is also reflected in the size of the frequency modulation in the radial directions, since it is larger for the x direction. It is important to note the order of magnitude of the frequency modulation, which is around 5kHz for the radial and 40kHz for the axial direction, in order to be able to compare to the experimental results.

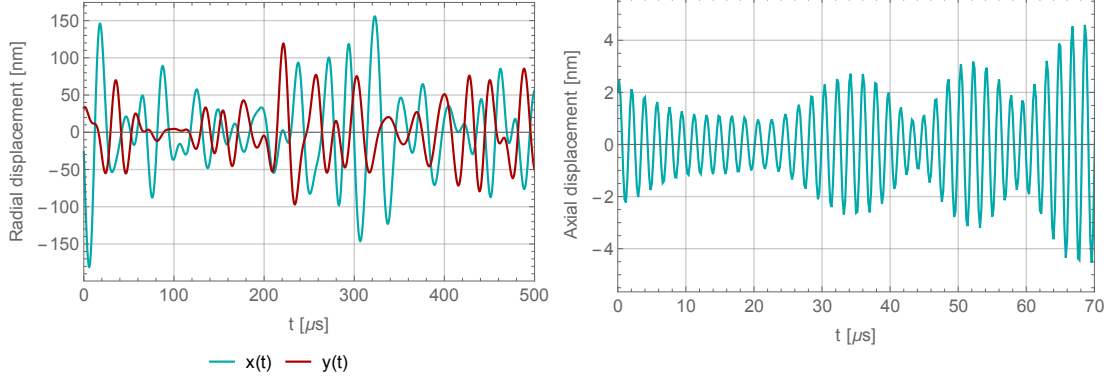
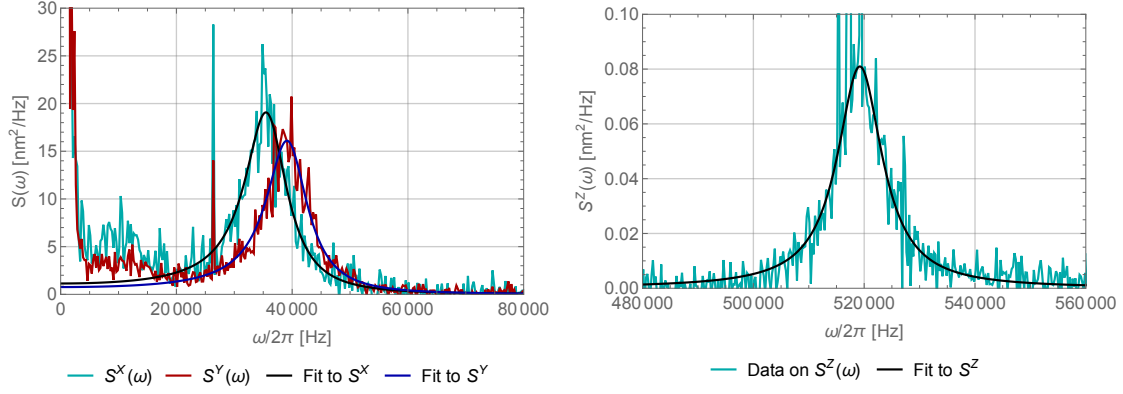


Figure 17: Time traces of the radial and axial motion of the particle at a pressure of 4.2mBar and a trapping beam power of 600mW. In post processing the recorded signal was digitally filtered, from 20-60kHz in radial and from 480-560kHz in axial direction, to decrease overlaid noise. For the calibration we use equation (50), with a temperature of 293K.

The corresponding noise power spectra of the full time traces are shown in figure 18, along with the theoretical fits to the data and corresponding fitting parameters. From these we can determine the ratio of the two radial frequencies with the axial frequency to be $\Omega_Z/\Omega_X = 14.4 \pm 0.1$ and $\Omega_Z/\Omega_Y = 13.1 \pm 0.1$. For a particle with a radius of 150nm, the damping constant given in equation (46) at 4.2mBar has a value of $\Gamma_0 \approx 7.8\text{kHz}$. Comparing this to the measured values shows reasonable similarity, although the values are slightly too high. A possible explanation of this is inhomogeneous broadening. This effect occurs in the case of intensity noise in the trapping laser, which again causes fluctuations of the frequency during the record of the time traces, and effectively broadens the peak.

Although the measured values for the frequencies are—compared to the theoretical values of the last subsection—in the right orders of magnitude, it is obvious that there is a huge discrepancy between the two. Even if one assumes artificially high uncertainties in the parameters that go into the calculation of the frequencies, and includes frequency elevating effects from a beating pattern in the potential (figure 16), the experimentally measured values can not be explained with the theoretical equations. This is a problem, that is so far unresolved.

It is reassuring though, that this concerns mainly an overall factor of the frequencies, since the qualitative behavior of trap and readout is in agreement with other experimental results. As we will see in 4.4.3, the functional dependence of the frequency on the power of the trapping beams, is in good agreement with equation (53). Furthermore, the beating pattern discussed in 4.3 will be experimentally verified and shows a good agreement with the theoretically predicted periodicity. And lastly, the ratio of the frequencies is in acceptable agreement with the theoretical value. Concluding we can therefore say, that the unexplainably high experimental values for the frequencies should not significantly



[kHz]	X	Y	Z
Ω_0	36.0 ± 0.2	39.6 ± 0.1	519.3 ± 0.2
Γ_0	8.9 ± 0.3	8.7 ± 0.2	9.9 ± 0.3

Figure 18: Power spectral densities of a particle with radius 150nm, at a pressure of 4.2mBar and a trapping beam power of 600mW. Electronic noise peaks are visible in the axial as well as radial direction. In addition to that, there is noise from the readout laser at lower frequencies in the radial directions, which explains the deviations from the fit. For the fit we used equation (49).

effect the validity of the theoretical model.

4.4.2. Pressure dependence of the Damping Constant

Equation (46) gives the pressure dependence of the damping constant, and is visualized in figure 15. By measuring the power spectral density of the particle motion at different pressures, we can experimentally test this relation in the setup. The range in which this measurement can be done is limited by two factors. First due to increasingly unresolvable particle peaks, starting at pressures around ~ 50 mBar, since the peak height diminishes with increasing line width, causing the peak to vanish in the noise. And second, since the particle is lost at pressures around ~ 1 mBar.

For the measurement we used a sphere specified with a radius of 127nm. The experimental data for the accessible range is visualized in figure 19 for one of the radial directions. A fit to the data, using the theoretically expected mathematical expression, shows that the measured results would require a particle radius of:

$$a_p = (225 \pm 2)\text{nm}$$

which is nearly twice the size specified by the manufacturer of the spheres. Furthermore, the fit requires an offset in the pressure

$$p_{\text{offset}} = (1.5 \pm 0.5)\text{mBar}$$

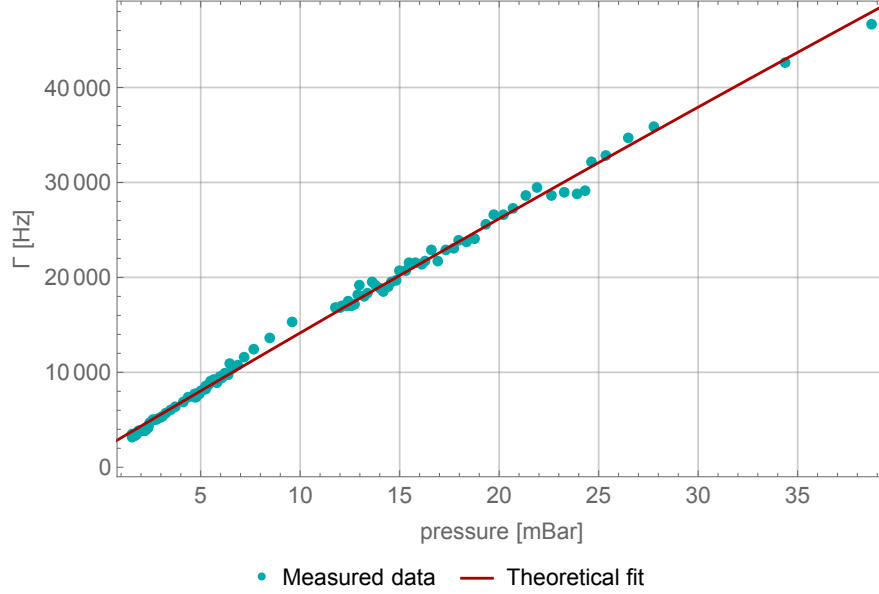


Figure 19: Pressure dependence of the damping factor Γ , as determined with the position readout in radial direction. The red line shows a fit to the data, using the theoretical dependence in equation (46).

in order to be in agreement with the theoretical expectation. The former could be due to clustering of the particles in the solution that is evaporated with the nebulizer. A factor of two in the radius corresponds to a factor of eight in volume, meaning that the measurement would actually have been done with a cluster of around eight particles. Besides clustering, it is also conceivable that dirt in the solvent sticks to the spheres surface, thereby leading to the deviance in the data. The offset in pressure can be caused by inhomogeneous broadening, which we already explained in the last subsection.

4.4.3. Power dependence of the Oscillation Frequency

In equation (53) of subsection 4.3, we see that the frequencies of the motion depend on the square root of the laser power. By using the AOMs to change the power of both trapping beams, while recording the power spectral densities of the radial motion, we can experimentally verify this relation. The Power was monitored with the same photodetector, that is used for the axial position readout.

Figure 20 shows the results of this measurement, for both radial directions. There is a good agreement between the experimental data and the theoretical fit. For the latter, we used the function $\Omega_{\text{rad}}(P) = f_{\text{conv}} \sqrt{c_{\text{noise}} + P}$, which includes an offset c_{noise} in the Power to cope for a constant noise floor in the photodetectors.

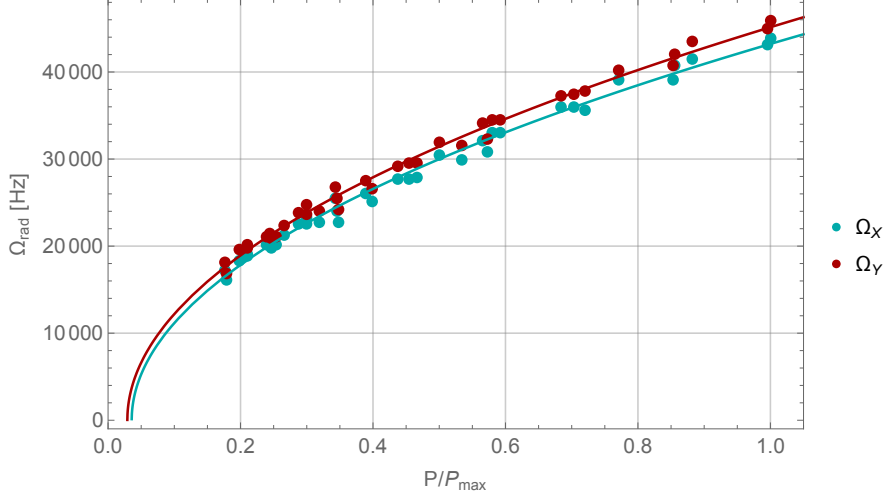


Figure 20: Power dependence of the oscillation frequencies for the radial particle motion. The lines in corresponding color show a fit to the data, that includes a slight offset in the power. This is necessary to cope for a constant noise floor in the photodetectors that are used to measure the power.

4.4.4. Spatial Beating Pattern of the Trapping Potential

As theoretically discussed in subsection 2.6 and 4.3, an excitation of higher order modes while coupling the trapping beam in the fiber, results in a periodic shift of the trapping potential as well as the frequency. This effect can indeed be observed in our setup, by characterizing the frequency of the trapping potential at different positions along the fiber axis.

Frequency Dependence on the Axial Position

The measurement is done, by translating the standing wave potential in incremental steps via the AOMs (as described in subsection 2.5.2). The step size depends on the time interval during which the frequency detuning is turned on, and was set to the smallest possible duration of (2.4 ± 0.1) ms. Using equation (24) for the speed of the standing wave, we can calculate the corresponding step size to be $\Delta s = (12.5 \pm 0.6)\mu\text{m}$. The measurement was done with a particle of radius $a_p = 150\text{nm}$ and a trapping beam power of 600mW. At each position, the time traces of the radial readout and a power spectrum of the axial readout were recorded. Figure 21 shows the results for this measurement.

The periodic nature of the behavior along the axis of the fiber is clearly visible in all directions of motion, and can also be seen in the autocorrelation function, in figure 22a) (see appendix A.2 for definitions). The average distances between the maxima, calculated from the data in figure 21, turn out to be:

$$\Delta z_x^\Omega = (79 \pm 7)\mu\text{m} \quad \Delta z_y^\Omega = (82 \pm 6)\mu\text{m} \quad \Delta z_z^\Omega = (80 \pm 9)\mu\text{m}$$

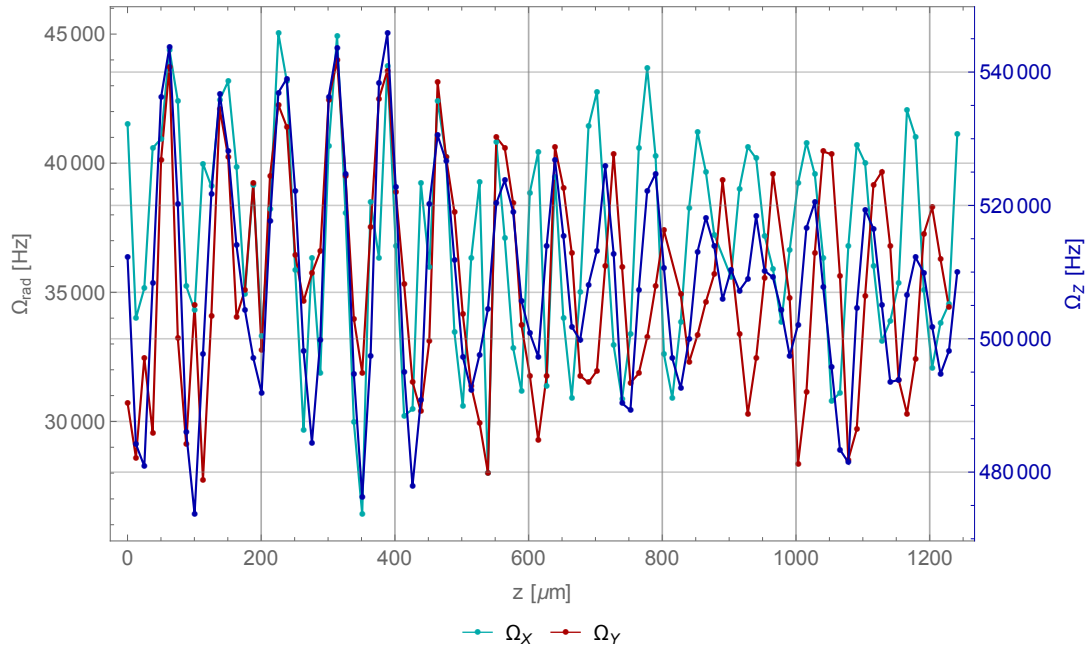


Figure 21: Frequencies of the trapping sites at different positions along the z axis. The measurement was done with a 150nm particle and a trapping beam power of 600mW. The distance between individual measurement points is $\Delta s = (12.5 \pm 0.6)\mu\text{m}$.

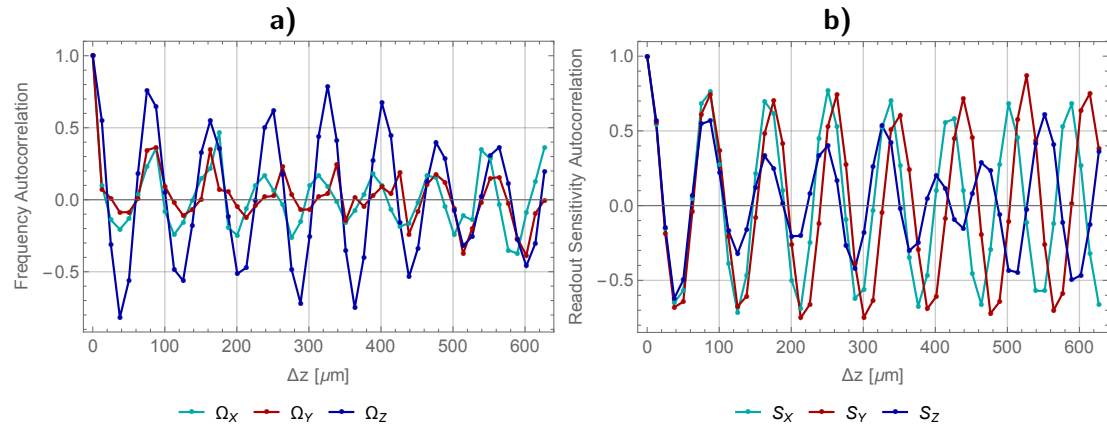


Figure 22: Autocorrelation function of the position dependent frequency as shown in figure 21 **a)** and the sensitivity of the readout as shown in figure 23 **b)**.

These values are clearly consistent and give a combined estimate on the periodicity of $\Delta z^\Omega = (80 \pm 2)\mu\text{m}$. From the theoretical calculations of subsection 2.6, the period is estimated to be $(104 \pm 21)\mu\text{m}$, where the uncertainty is calculated from the HCPCF specs on the fiber radius a_c (see appendix A.3). This shows a reasonable agreement of both values, while suggesting, that the radius of the fiber core is actually at the lower end of the uncertainty range.

An unexpected behavior can be seen in the relative phases between the different directions of oscillation. As it seems, the frequencies start in phase and then drift apart over the length of the measurement. This drift is strongest between the two radial directions, which can also be seen by looking at the correlations in table 1. From the theoretical

$C(\Omega_i, \Omega_j)$	Ω_y	Ω_z	$C(S_i, S_j)$	S_y	S_z
Ω_x	0.04	0.34	S_x	0.47	-0.07
Ω_y	1	0.35	S_y	1	0.35

Table 1: Correlation between the different directions of the readout for the frequency and sensitivity of the readout.

discussion we would expect all three directions to be in phase, which is only true for roughly the first three beating periods. Therefore there must exist additional effects, which cause the dephasing.

The frequency of the trap depends on the potential shape and depth, and since the depth is always the same for all three directions, it is clear that it must be a periodic change of the potential shape, with inverse effects for x and y. It is conceivable, that this is due to a more complicated interference pattern than the one discussed in subsection 2.6, caused by two different superpositions of the degenerate LP_{11} modes. For further analysis, it would therefore be necessary to measure the spatial intensity distribution of the trapping lasers at both fiber ends, in order to learn more about the modes to which the light is coupled.

Another possible cause of the dephasing could be birefringence of the hollow core photonic crystal fiber, for the two orthogonal LP_{11} modes. This seems plausible, since the fiber has a natural asymmetry due to the hexagonal shape of the photonic crystal, as can be seen in the data sheet (see appendix A.3). A slightly different wave vector due to the birefringence between the two LP_{11} modes, would cause a beating of the interference pattern and respectively the trapping potential. Since this would also effect the axial readout, it could result in the effect we see in the data, i.e. the modulation of the radial frequencies being in phase in some places and out of phase in others, with the axial frequencies being in between. In the light of the results for the sensitivity of the readout though, which we discuss in the following, and where we find a reasonable correlation between the radial directions, the birefringence seems less promising as an explanation, since it should lead to dephasing there as well.

Finally, the dephasing could also be simply due to local impurities in the fiber, either from dirt that is introduced during the suction of the evaporated particles, or from the manufacturing process. This could have an influence on the shape of the trapping

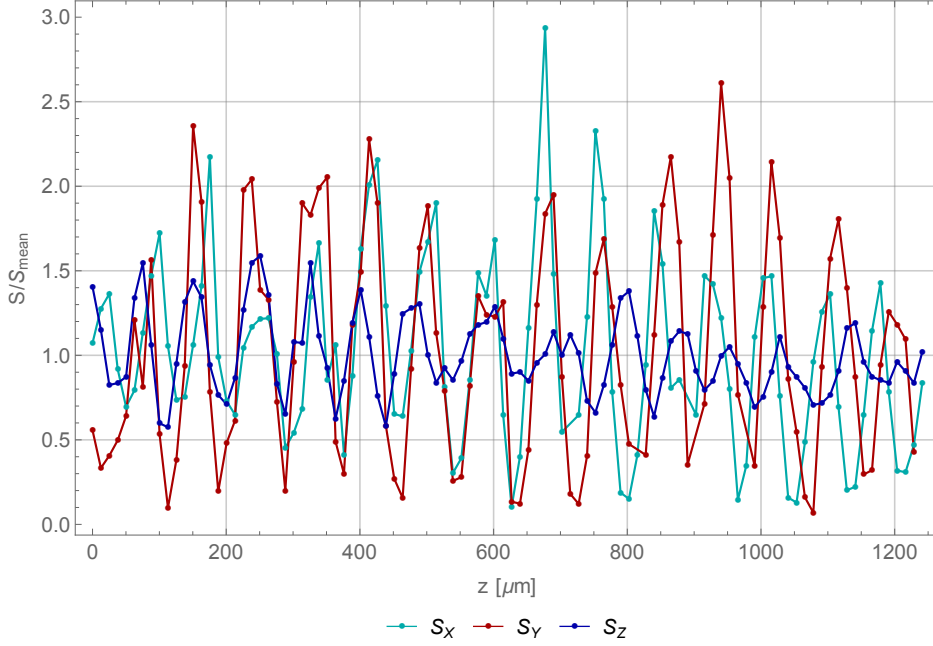


Figure 23: Readout sensitivity dependence on the axial position in the fiber. The data comes from the same measurement run as the results in figure 21. For better comparison between the three directions, the data was normalized by the mean value of the traces.

potential and thereby disturb the expected pattern of the frequencies.

Sensitivity of the Detection

Looking back at equation (40), which gives a quantity that is proportional to the expected signal of the radial detection, we see that this is also dependent on the axial position via the cosine term. It shows a periodic modulation of the sensitivity of the readout, with a period that is equal to that of the trapping potential beating pattern. Changing the sensitivity affects the size of the signal and therefore the height of the particle peaks in the corresponding power spectral densities, resulting in the same effect as if one changes the temperature of the surrounding heat bath. If we assume the temperature to be constant during the measurement, the size of the peaks acts as indicators for the readout sensitivity and can be obtained from a fit to the data.

Figure 23 shows the results on the sensitivity for all three readout directions, normalized by the mean values of the data. As for the frequencies, the periodic behavior is clearly visible and again quantified by the autocorrelation functions, which can be found in figure 22b). The extracted mean values for the period of the individual directions are:

$$\Delta z_x^S = (83 \pm 5)\mu\text{m} \quad \Delta z_y^S = (86 \pm 10)\mu\text{m} \quad \Delta z_z^S = (88 \pm 15)\mu\text{m}$$

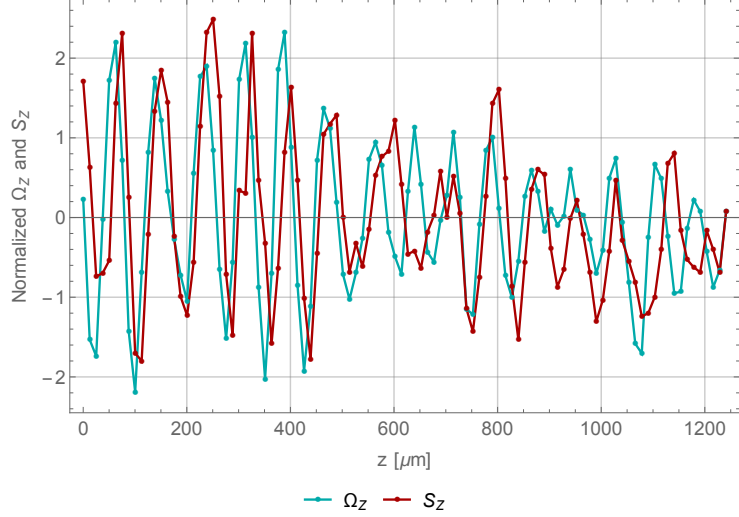


Figure 24: Correlation of the axial frequencies with the readout sensitivity. The data was normalized according to $\tilde{f}_i = \frac{f_i - \bar{f}}{\sigma(f)}$. The correlation was calculated to be $C(\Omega_Z, T_Z) = 0.5$. This is in good agreement with the theoretical expectations, since the periodic depth of the trapping potential influences the frequency and power that is radiated by the particle.

As before for the frequency modulation, these values are consistent among themselves. Also, the combined estimate on the period $\Delta z^S = (86 \pm 3)$ is in agreement with the results for the frequency modulation. This backs the theoretical explanation, that both the trapping potential and the readout sensitivity, show a periodic modulation due to the different wave vectors of the guiding modes.

It might be puzzling, that the readout in axial direction shows a modulation of the sensitivity as well, even though there is no periodic z -dependence in equation (42). This can be explained though, since the sensitivity also depends on the optical power that is radiated by the particle and its coupling to the LP_{01} mode, which again depend on the intensity at the trapping position and the radial displacement. Since the laser that is used for the axial readout is the same as the trapping laser, the modulation of the optical potential due to the beating is forwarded to the radiated power, and thereby to the sensitivity of the axial detection. This is also in agreement with the fact that the modulation for the axial direction is smaller than for the radial direction, and shows good correlation with the modulation of the frequency, as can be seen in figure 24. The correlation was calculated to be $C(\Omega_Z, T_Z) = 0.5$. There are two possible explanations for non conformities in the modulation of Ω_Z and S_Z . On the one hand, intensity noise in the light reaching the photodetector has an influence on the size of the signal and thereby the sensitivity, and on the other hand the usual beating pattern of the potential can be altered by e.g. dirt in the fiber, with different effects on sensitivity and frequency.

4.5. Damping by Active Feedback on the Optical Potential

Feedback cooling of suspended micron- and nano-sized particles was already demonstrated several times (Ashkin and Dziedzic, 1977; Li et al., 2011; Gieseler et al., 2012), and can be seen as state of the art in the field of optical levitation. So far though, such a scheme has not been reported for an optical trap inside a hollow core photonic crystal fiber. This subsection discusses preliminary data and a partial success in the cooling of the center of mass motion.

4.5.1. Formal Description

The implementation of the cooling in our setup is denoted as *parametric feedback*. Its principle idea is, to use the information on the particle motion from the optical readout, to actively modulate the power of the trapping beams—and thereby the spring constant that describes the potential—to achieve a counteracting force on the particle, which slows the particle down and thus cools the center of mass motion. In this thesis we concentrate on an intuitive motivation of the subject, while a more detailed theoretical treatment can be found in (Gieseler, 2013).

As seen in subsection 4.3, the frequencies of the trapping potential depend on the square root of the trapping beam powers (eq. (53)). The spring constant, and respectively the squared frequency ($\Omega_0 = \sqrt{\kappa/M}$) in the Langevin equation, are therefore linearly dependent on the power. A small modulation on a constant offset of the power, leads therefore to an additional force in the Langevin equation, whose maximum size depends on the amplitude of the modulation:

$$\frac{d^2x}{dt^2} + \gamma \frac{dx}{dt} + (\Omega_0^2 + \underbrace{\Delta\Omega^2(t)}_{=:F_{fb}(t)})x = F_{\text{therm}}(t) \quad (54)$$

One possible implementation of the feedback, is to use the time derivative of the squared amplitude of the particle motion: $\Delta\Omega^2(t) \propto 2x\dot{x}$ for the modulation of the potential. This can be easily illustrated for the case of a particle that oscillates with an amplitude $x(t) = a \cos(\Omega_0 t)$. As can be seen in figure 25a), the signal modulating the power increases the optical potential every time the particle moves in an outward direction, and decreases it if the particle is oscillating back. The result is an additional force that opposes the movement of the particle. It can be shown (Gieseler et al., 2012), that the effect of the feedback results in an additional damping $\Delta\Gamma$ and frequency term $\Delta\Omega$ in the power spectral density of the particle:

$$S(\omega) = \frac{2k_B T}{M} \frac{\Gamma_0}{([\Omega_0 + \Delta\Omega]^2 - \omega^2)^2 + \omega^2[\Gamma_0 + \Delta\Gamma]^2} \quad (55)$$

By integrating the power spectral density, we can derive the mean square displacement of the cooled particle:

$$\langle x^2 \rangle = \frac{k_B T}{M(\Omega_0 + \Delta\Omega)^2} \frac{\Gamma_0}{\Gamma_0 + \Delta\Gamma} \quad (56)$$

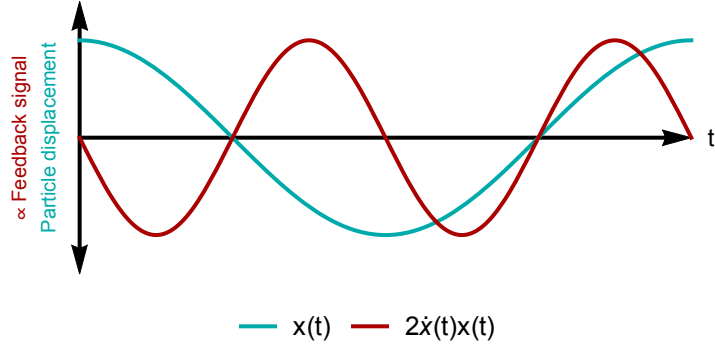


Figure 25: Illustration of the applied feedback signal, which modulates the power of the trapping beams and thereby the depth of the optical potential.

The shift of the frequency is much smaller than the frequency itself $\Delta\Omega \ll \Omega_0$. Looking at the last equation and comparing it with its analog for the case without applied feedback modulation (equation (50)), we therefore see, that it is possible to define a new effective temperature T_{eff} for the cooled particle:

$$T_{\text{eff}} = T \frac{\Gamma_0}{\Gamma_0 + \Delta\Gamma} \quad (57)$$

Where $\frac{\Gamma_0}{\Gamma_0 + \Delta\Gamma} =: f_{\text{cl}}$ is denoted as cooling ratio. This can be seen as the temperature, that the surrounding medium would have to have, in order for the mean square displacement of the particle to have the same size as in the case of applied feedback cooling. Using this new definitions, we rewrite expression (55) for the power spectral density of a cooled particle:

$$S(\omega) = \frac{2k_{\text{B}}T_{\text{eff}}}{M} \frac{\Gamma_{\text{eff}}}{(\Omega_{\text{eff}}^2 - \omega^2)^2 + \omega^2\Gamma_{\text{eff}}^2} \quad (58)$$

Where we rewrote $\Gamma_{\text{eff}} = \Gamma_0 + \Delta\Gamma$ and $\Omega_{\text{eff}} = \Omega_0 + \Delta\Omega$. As we can see, it is possible to use the same theoretical expression for the power spectral density as in the case without feedback cooling, as long as one interprets the parameters as the corresponding effective quantities. It is important to note, that by choosing the right phase of the applied feedback modulation, the sign of $\Delta\Gamma$ can become negative, thereby causing a heating of the particle motion.

4.5.2. Experimental Results

Due to technical reasons and problems, the feedback cooling was so far only done in one radial direction, meaning that only the particle signal of the x direction was used to create the signal for the power modulation. Here we will discuss the effect of the modulation on both radial directions of the particle.

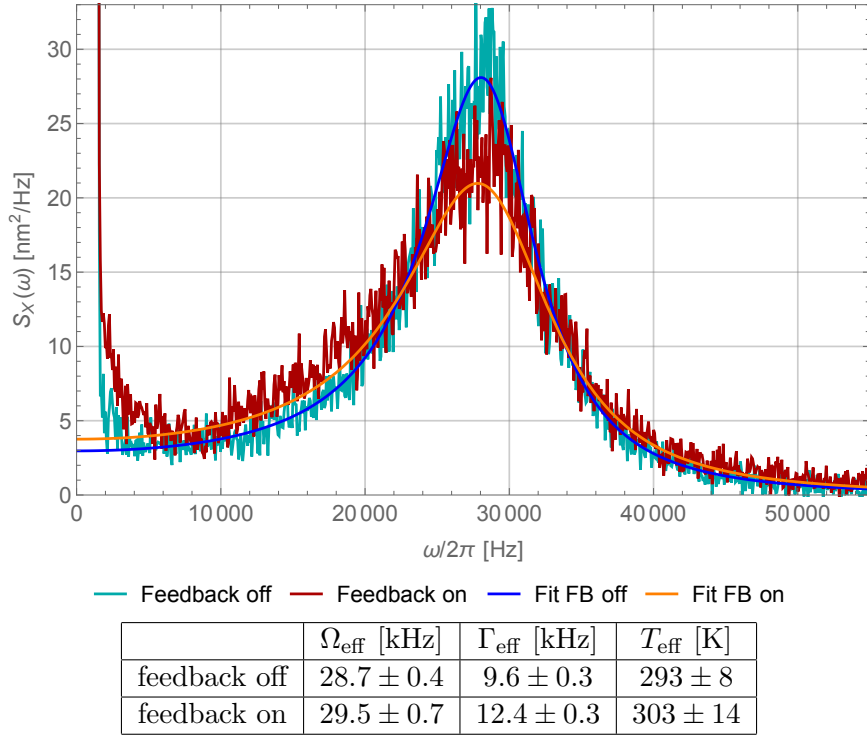


Figure 26: Two power spectral densities of the radial motion of a particle trapped at a pressure of (5.3 ± 1.6) mBar, with a trapping beam power of 600mW. The blue line shows the normal trapping case, and the red line the case of applied feedback cooling. Averaged fitting parameters from a repetition of on/off cycles are shown in the lower table.

Figure 26 shows two power spectral densities of the motion in x -direction, of a particle trapped at a pressure of (5.3 ± 1.6) mBar with a trapping beam power of 600mW. One reflects the normal motion in the trapping potential, while the other shows the case of applied feedback cooling. Although small, an effect is clearly visible. From a fit to the data we obtain the parameters of the peaks, which we average over repeated on/off cycles and show in the table below the power spectral densities. From the results on the line width broadening, we can calculate the cooling ratio of the applied feedback, and the effective temperature of the cooled center of mass motion of the particle (see equation (57)):

$$f_{\text{cl}} = (0.77 \pm 0.03) \quad T_{\text{eff}} = (226 \pm 8)\text{K} \quad (59)$$

The room temperature was taken to be (293 ± 2) K. As we see, the line width behaves as expected in the case of feedback cooling.

To verify that the particle motion is actually cooled, it is necessary to look at the area under particle peaks. According to equation (56), this is proportional to the temperature of the surrounding medium T , and in the case of applied feedback to the effective temperature T_{eff} . The cooling ratio f_{cl} can therefore also be calculated from the ratio of the areas under the peaks, which themselves can be taken from the fit parameters. The calibrated experimental mean values on T_{eff} can be found in the table in figure 26, from which the cooling ratio can be calculated to be:

$$f_{\text{cl}} = (1.03 \pm 0.05)$$

This represents a strong discrepancy with results that were found before, and does not even constitute cooling any more. Before we go into a discussion of possible causes, it is also interesting to see whether the feedback modulation has any effect on the particle motion in y direction. Two examples of power spectral densities of the particle motion in y direction are shown in figure 27, and were recorded simultaneously with the peaks in figure 26. As before, the parameters from fits to the data are averaged over several on/off cycles, and shown in table below the power spectral densities.

As can be seen, there is no visible effect on the oscillation frequency Ω_{eff} or the line width Γ_{eff} of the peaks, which is what we expect since the feedback signal applies to the motion in x direction. Considering the effective temperature of the particle though, the parameters again imply a heating of the particle motion. This heating effect in both radial directions poses a problem, that is so far unresolved and currently the limiting factor of the setup.

There are two possible reasons that we consider as a cause of the effect. One is additional noise on the applied feedback modulation, due to the technical implementation of the signal processing. This would stochastically drive the particle motion, thereby heating it, and would be consistent with the effects we observe for the x and y readout. The additional effect on the line width of the x readout, could then be due to an actual cooling of the motion, which is though not observable in the effective temperature, since it is covered by the effect of the noise. Again this would be consistent with the measured data, since for applied feedback, the observed effective temperature T_{eff} of x is smaller than of y .

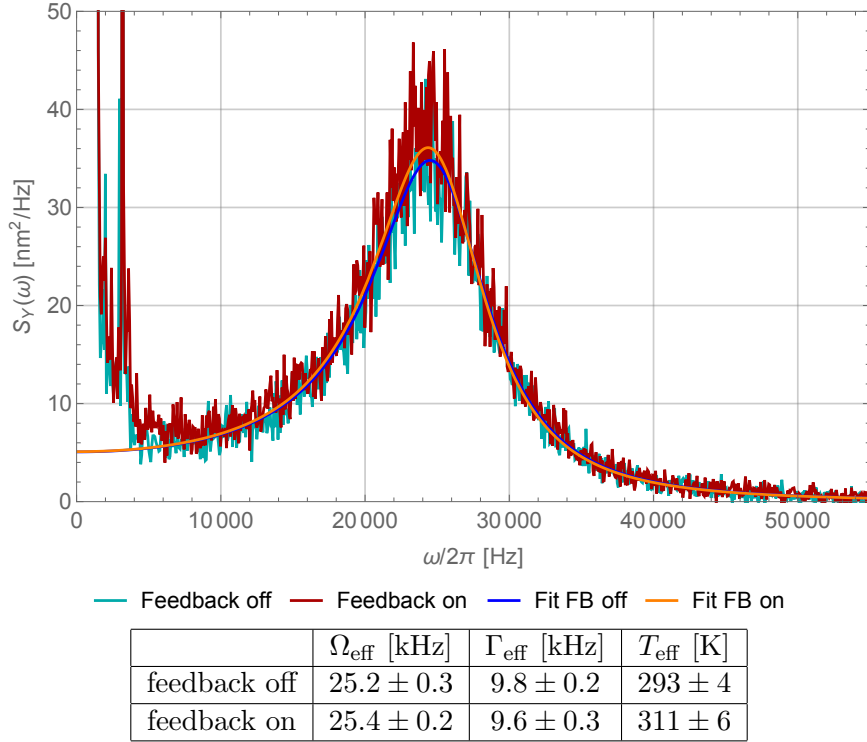


Figure 27: Power spectral densities of the particle motion in y -direction, corresponding to the peaks in figure 26. The fitting parameters given in the lower table, are averaged over multiple on/off cycles of the feedback modulation.

Another possible cause of the observed heating, could be due to the technically unavoidable delay, with which the feedback modulation is applied to the particle motion. This has a nonlinear dependence on the frequency of the modulation, which for peaks as broad as in our case, has the effect that in some frequency ranges the applied modulation is out of phase with the particle motion. Since the delay is adjusted to be in phase with the main frequency Ω_0 , this results in cooling of the center of the peak, and possible heating of the outer parts. This effect is not covered by the theoretical expression of the power spectral density (58), which causes a mismatch in the fit of the data. In figure 26, the poor agreement of fit and data in the case of applied feedback, allows to suspect that such an effect indeed plays a role. Since the effective temperature T_{eff} is determined from the parameters of the fit, the effect of the varying delay could also cause the inconsistencies in the results.

5. Summary and Outlook

In the course of the work on this thesis, great advances were made towards the final goal of a feedback cooled particle loading mechanism. Trapping and translation of particles inside the hollow core fiber, are now well established methods, and were routinely used in the course of this thesis. In addition to that, we achieved a three dimensional readout of particles inside the fiber, that is sensitive enough to resolve the thermal motion of the particle. We developed a theoretical model of the readout and trapping mechanisms, that provide a qualitative understanding of the system, and allow for estimates on experimentally important quantities. Finally, active feedback was successfully demonstrated to provide damping of the particle motion, and with it the principal possibility of three dimensional cooling.

The next step on the setup is now to get rid of the additional heating by the activated feedback in order to achieve cooling. The scheme can then be extended to both radial directions, which finally allows to check whether two dimensional feedback cooling on the radial motion is indeed sufficient, to counteract the loss mechanism during the evacuation of the fiber. The outcome of this determines, whether it is necessary to extend the feedback cooling to the axial motion. Concluding one can say, that a working loading mechanism for ultra high vacuum purposes is within reach.

We also want to highlight some of the interesting possibilities that a HCPCF trapping setup enables. One of them is the continuous translation of particles in axial direction. Although our setup only uses this on a scale of centimeters, the small attenuation of $< 0.1\text{dB/m}$ in the HCPCF, would in principle allow an extension to a scale of 10 meters. Furthermore, the core of a HCPCF can be seen as one of the probably smallest vacuum chambers to exist, which in addition to that can be used to bridge pressure differences of nine orders of magnitude. The small size of the HCPCF make it possible to place experimental equipment near the trapped particle, within a distance of $\simeq 110\mu\text{m}$, and could for example be used to electromagnetically exert forces on charged particles. Lastly, the reduced complexity of the setup compared to a trap inside a cavity for example, gives it a huge practical advantage. Generally one can say, that the unique properties of a particle trap inside a HCPCF, make it a promising candidate for new applications in different fields.

A. Appendix

A.1. Optical Forces

A.1.1. Maxwell Equations

$$\begin{aligned}\nabla \cdot \mathbf{E} &= \frac{1}{\epsilon_0} \rho \\ \nabla \cdot \mathbf{B} &= 0 \\ \nabla \times \mathbf{E} &= -\frac{\partial \mathbf{B}}{\partial t} \\ \nabla \times \mathbf{B} &= \frac{1}{c^2} \frac{\partial \mathbf{E}}{\partial t} + \mu_0 \mathbf{j}\end{aligned}$$

A.1.2. Products of Harmonic Fields

The following relation holds for a product of two harmonic fields in complex notation (Jackson, 1999):

$$\begin{aligned}\mathbf{J}(\mathbf{r}, t) \cdot \mathbf{K}(\mathbf{r}, t) &= \text{Re}\{\tilde{\mathbf{J}}(\mathbf{r})e^{-i\omega t}\} \cdot \text{Re}\{\tilde{\mathbf{K}}(\mathbf{r})e^{-i\omega t}\} \\ &= \frac{1}{4} \left(\tilde{\mathbf{J}}(\mathbf{r})e^{-i\omega t} + \tilde{\mathbf{J}}(\mathbf{r})^*e^{i\omega t} \right) \cdot \left(\tilde{\mathbf{K}}(\mathbf{r})e^{-i\omega t} + \tilde{\mathbf{K}}(\mathbf{r})^*e^{i\omega t} \right) \\ &= \frac{1}{2} \text{Re} \left\{ \tilde{\mathbf{J}}^*(\mathbf{r}) \cdot \tilde{\mathbf{K}}(\mathbf{r}) + \tilde{\mathbf{J}}(\mathbf{r}) \cdot \tilde{\mathbf{K}}(\mathbf{r})e^{-2i\omega t} \right\}\end{aligned}$$

A.1.3. Dipole Approximation

We have

$$\begin{aligned}\dot{\mathbf{p}} \times \mathbf{B} &= \frac{d}{dt} (\mathbf{p} \times \mathbf{B}) - \mathbf{p} \times \frac{d\mathbf{B}}{dt} \\ &= \frac{d}{dt} (\mathbf{p} \times \mathbf{B}) + \mathbf{p} \times (\nabla \times \mathbf{E})\end{aligned}$$

where in the second line we have used the Maxwell equation for the curl of the electric field, and the approximation $\frac{d\mathbf{B}}{dt} = \frac{\partial \mathbf{B}}{\partial t}$ since the motion of the particle is much smaller than c . With this relation, and using a vector calculus identity that one can easily verify, the force turns out to be:

$$\begin{aligned}\mathbf{F}_{\text{dip}} &= (\mathbf{p} \cdot \nabla) \mathbf{E} + \dot{\mathbf{p}} \times \mathbf{B} \\ &= (\mathbf{p} \cdot \nabla) \mathbf{E} + \mathbf{p} \times (\nabla \times \mathbf{E}) + \frac{d}{dt} (\mathbf{p} \times \mathbf{B}) \\ &= \sum_i p_i \nabla E_i + \frac{d}{dt} (\mathbf{p} \times \mathbf{B})\end{aligned}$$

A.1.4. Modes of Free Space Propagation and the Gaussian Beam

As shown in (Saleh and Teich, 2007), the propagation of laser beams in free space can be described by the so called *Hermite–Gaussian* beams. The complex amplitudes of the electric fields of these beams are given by:

$$\begin{aligned} \tilde{\mathbf{E}}_{lm}(\mathbf{r}) = & \sqrt{\frac{2P}{c\epsilon_0}} \eta_{lm} \left(\frac{W_0}{W(z)} \right) \mathcal{H}_l \left(\frac{\sqrt{2}x}{W(z)} \right) \mathcal{H}_m \left(\frac{\sqrt{2}y}{W(z)} \right) e^{-\frac{x^2+y^2}{W^2(z)}} \\ & \times e^{-i \left(kz + k \frac{x^2+y^2}{2R(z)} - (l+m+1)\zeta(z) \right)} \end{aligned} \quad (60)$$

Where P is the power transmitted by the beam, η_{lm} is a normalization constant, \mathcal{H}_k are the Hermite polynomials and k is the wave vector. The other functions are defined as follows:

$$\begin{aligned} W(z) &= W_0 \sqrt{1 + \left(\frac{z}{z_0} \right)^2} & R(z) &= z \left(1 + \left(\frac{z_0}{z} \right)^2 \right) \\ \zeta(z) &= \arctan \left(\frac{z}{z_0} \right) & W_0 &= \sqrt{\frac{\lambda z_0}{\pi}} \end{aligned}$$

For the understanding of this thesis, only the first two of these modes are needed and we will state their complex amplitudes explicitly. The fundamental $\tilde{\mathbf{E}}_{00}(\mathbf{r})$ mode is also called *Gaussian beam* and described by:

$$\tilde{\mathbf{E}}_{00}(\mathbf{r}) = 2 \sqrt{\frac{P}{\pi c \epsilon_0}} \frac{1}{W(z)} e^{-\frac{x^2+y^2}{W^2(z)}} e^{-i \left(kz + k \frac{x^2+y^2}{2R(z)} - \zeta(z) \right)} \quad (61)$$

The first higher order mode, which resembles the LP₁₁ mode is given by:

$$\tilde{\mathbf{E}}_{10}(\mathbf{r}) = \sqrt{\frac{2P}{\pi c \epsilon_0}} \frac{1}{W(z)} x e^{-\frac{x^2+y^2}{W^2(z)}} e^{-i \left(kz + k \frac{x^2+y^2}{2R(z)} - 2\zeta(z) \right)} \quad (62)$$

A plot of the spatial part of the modes is given in figure 29. To illustrate the difference to the LP modes, they are only plotted until a radius that would correspond to the fiber core walls for a comparable LP mode.

Figure 28 illustrates the properties of gaussian beams, which are important for the calculations in this thesis. W_0 is called the *waist of the beam* and is the radial distance from the focus, where the intensity drops by a factor of e^{-2} . z_0 is called *Rayleigh length* and denotes the distance in axial direction from the focus, where the power transmitted through a circle with radius W_0 around the axis drops by $\frac{1}{2}$. Most importantly, the cone that specifies the divergence of the beam is given by the angle:

$$\theta_{\text{div}} = \frac{\lambda}{\pi W_0} \quad (63)$$

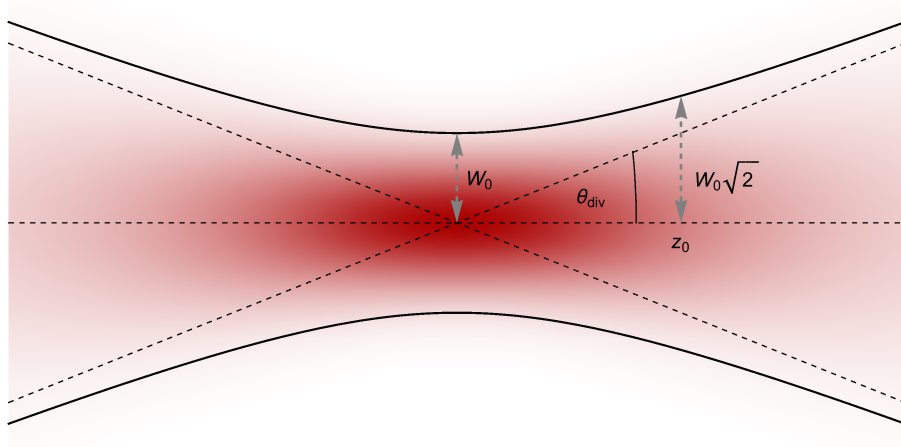


Figure 28: Illustration of the properties of a gaussian beam that are important for the understanding of this thesis. W_0 is the waist of the beam, z_0 the Rayleigh-length and θ_{div} the angle of divergence.

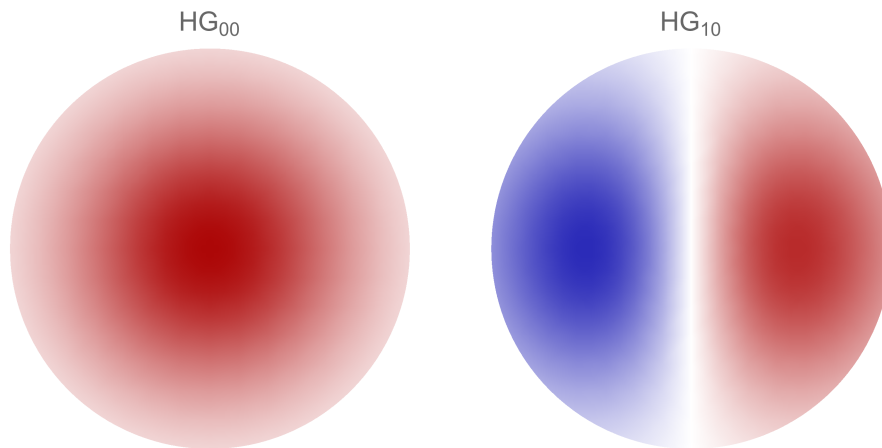


Figure 29: Illustration of the spatial form of the Hermit-Gaussian beams. The plot show the complex amplitude of the electric field without the phase factor. Red denotes positive and blue negative values. To highlight the difference to the LP modes, the plots are cut at a radius that would correspond to the walls of the fiber core for a comparable LP mode.

A.2. Correlation and Autocorrelation Function

The correlation of two signals $f(t)$ and $q(t)$ is defined as:

$$C(f, q) := \frac{\langle f' \cdot q' \rangle}{\langle f'^2 \rangle \langle q'^2 \rangle} \quad \text{with} \quad \langle f' \rangle = f - \langle f \rangle \quad (64)$$

The autocorrelation function is then given by the correlation of the signal with itself, shifted by an amount τ :

$$C_f^{\text{auto}}(\tau) = C(f(t), f(t + \tau)) \quad (65)$$

For experimental time traces with finite length N and discrete data points v_n recorded at times Δtn , we can only evaluate the autocorrelation function for discrete shifts $\tau = \Delta tm$. In this thesis, $C_v^{\text{auto}}(\Delta tm)$ is then determined by calculating the correlation of the two reduced value series:

$$v_i \quad \text{for} \quad i = \{m, m+1, \dots, N-1, N\} \quad \text{and} \quad \tilde{v}_i \quad \text{for} \quad i = \{1, \dots, N-(m+1), N-m\}$$

This is necessary, because every shift produces “end pieces” that have no well defined phase relation to each other.

A.3. Datasheet on the Hollow Core Fiber



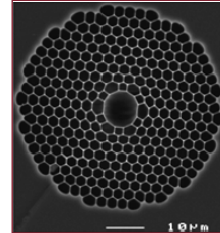
Crystal Fibre • *aeroLASE* • Koheras • SuperK

HC-1060-02

Hollow Core Photonic Bandgap Fiber for 1060nm Range Applications



- >95% of optical power located in air
- Quasi-Gaussian fundamental mode
- Can be filled with gas
- Low bend loss down to few mm bend radius
- Fresnel reflection to air at the end faces $<10^{-4}$
- Up to 80% of fiber cross section composed of solid silica, facilitating fusion splicing to conventional fibers
- Undoped silica for good temperature stability



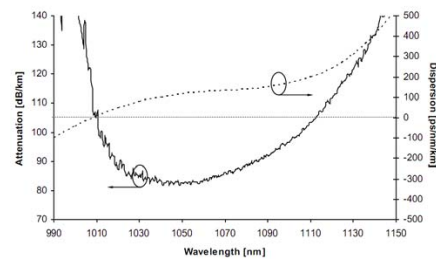
Hollow core photonic bandgap fibers guide light in a hollow core surrounded by a microstructured cladding formed by a periodic arrangement of air holes in silica.

Since only a small fraction of light propagates in glass, the effect of material nonlinearities is significantly reduced and the fibers do not suffer from the same loss limitations as fibers made from all solid material.

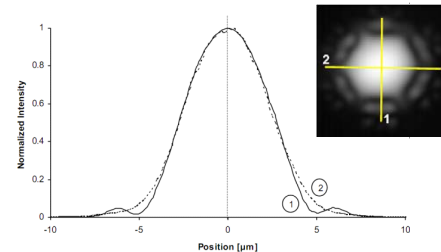
Applications include power delivery, pulse shaping and compression, sensors and nonlinear optics.

Physical properties	
Core diameter*	10 $\mu\text{m} \pm 1 \mu\text{m}$
Pitch	2.75 μm
Air filling fraction PBG region	> 90%
Diameter of holey region	50 μm
Cladding diameter	123 $\mu\text{m} \pm 5 \mu\text{m}$
Coating diameter (single layer acrylate)	220 $\mu\text{m} \pm 50 \mu\text{m}$
Optical properties	
Center wavelength	1060 nm
Attenuation @ 1060 nm	< 0.1 dB/m
Dispersion @ 1060 nm	120 ps/nm/km
Dispersion slope @ 1060 nm	1 ps/nm ² /km
Dispersion slope @ zero disp. wavelength	4.4 ps/nm ² /km
10 dB width of transmission band	> 90 nm
Fraction of light in air	> 90%
Mode field diameter ($1/e^2$)	7.5 $\mu\text{m} \pm 1 \mu\text{m}$
Effective mode index	~0.99
Mode shape overlap with std. SMF	> 90%

Typical attenuation and dispersion



Typical near field intensity



* Core formed by removing 7 hexagonal unit cells of the cladding

HC-1060-02-100409

NKT Photonics A/S (Headquarters)
 Blokken 84 • 3460 Birkerød • Denmark
 Phone: +45 4348 3900
 Fax: +45 4348 3901
www.nktphotonics.com

NKT Photonics GmbH
 Schanzenstrasse 39 • Bldg D9-D13
 51063 Cologne • Germany
 Phone: +49 221 99511-0
 Fax: +49 221 99511-650

NKT Photonics Inc.
 1400 Campus Drive West • Morganville
 NJ 07751 • USA
 Phone: +1 732 972 9937
 Fax: +1 732 414 4094

B. Zusammenfassung

Diese Arbeit baut auf den Ergebnissen der Masterarbeit von David Grass (Grass, 2013) auf und beschäftigt sich mit der Detektion der Massenmittelpunktsbewegung von Silikat Nanoteilchen in der optischen Falle einer Hohlkernfaser und deren Kühlung durch einen parametrischen Regelkreis. Die erfolgreiche Detektion aller drei Translationsfreiheitsgrade, sowie vorläufige Ergebnisse der Kühlung in einer der radialen Dimensionen der Teilchenbewegung werden demonstriert. Das Ziel ist es, mit Hilfe der Kühlung kritische Druckbereiche beim abpumpen der Vakuumkammern zu überbrücken, damit das Teilchen in ein Druckregime im Bereich von 10^{-3} mBar gebracht werden kann.

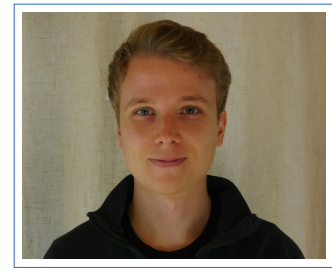
Der nötige theoretische Hintergrund der optischen Falle, sowie der speziellen Eigenschaften der Hohlkernfaser werden erläutert und schließlich der physikalische Mechanismus der Bewegungsdetektion in allen drei Raumrichtungen diskutiert. Im Anschluss wird die Brownsche Bewegung der Nanoteilchen und deren Charakteristik in der optischen Falle besprochen. Die im Experiment gemessenen Daten der Teilchenbewegung, werden mit den theoretischen Vorhersagen verglichen und es zeigt sich eine vernünftige Übereinstimmung. Schlussendlich werden der theoretische Hintergrund, die Implementierung und die erwarteten Effekte der parametrischen Kühlung erklärt und mit den experimentellen Resultaten verglichen.

C. Curriculum Vitae

See next page.

Julian Fesel

B.Sc.



Personal data

Date of birth 10.06.1989

Nationality Austria

Education

- 10/2012 – today **Master's studies of Physics**, *University of Vienna, Faculty of physics, Vienna.*
- 10/2009 – 10/2012 **Bachelor's studies of Physics**, *University of Vienna, Faculty of physics, Vienna.*
Bachelor's thesis: "The EPR-Paradox and the Bell-Inequality"
Graduated with distinction
- 10/2008 – 12/2008 **Training as Emergency medical technician**, *Civilian service – Red Cross, Salzburg.*
- 09/2003 – 07/2008 **Secondary School**, *Bundesgymnasium Seekirchen, Salzburg.*
Graduated with distinction
- 09/2001 – 07/2003 **Secondary School**, *Akademisches Gymnasium, Salzburg.*
- 09/1995 – 07/2001 **Elementary school**, *Rif-Rehhof, Salzburg.*

Bachelor's thesis

Title "The EPR-Paradox and the Bell-Inequality"

Written in the context of a seminar on theoretical quantum mechanics.

Working experience

- 2014 **Research Assistant in the Group of Prof. Aspelmeyer**, *University of Vienna.*
- 2014 **Tutor for "Theoretical Quantum Mechanics 1"**, *University of Vienna.*
- 12/2008-07/2009 **Emergency medical technician (7 months)**, *Red Cross, Salzburg.*
Civilian service as an EMT for the rescue service in Salzburg.
- 2005-2009 **Traineeship (5 months)**, *Palfinger AG, Salzburg.*
Assistance in the accounts department.
- 2009 **Traineeship (1 month)**, *Hypo-bank, Salzburg.*
Assistance in the property management.

Leisure interests

- Music I am learning to play the flamenco guitar and singing in the choir of the university of Vienna.
- Calligraphy On occasion I write postcards, letters or small poems calligraphically.
- Sport I do a fair amount of sport. Mostly jogging, swimming and weight training.

References

- A Ashkin. Acceleration and Trapping of Particles by Radiation Pressure. *Phys. Rev. Lett.*, 24(4):156–159, 1970a. doi: 10.1103/PhysRevLett.24.156. URL <http://link.aps.org/doi/10.1103/PhysRevLett.24.156>.
- A Ashkin. Atomic-Beam Deflection by Resonance-Radiation Pressure. *Phys. Rev. Lett.*, 25(19):1321–1324, November 1970b. doi: 10.1103/PhysRevLett.25.1321. URL <http://link.aps.org/doi/10.1103/PhysRevLett.25.1321>.
- A. Ashkin and J. M. Dziedzic. Feedback stabilization of optically levitated particles. *Applied Physics Letters*, 30(4):202, August 1977. ISSN 00036951. doi: 10.1063/1.89335. URL <http://scitation.aip.org/content/aip/journal/apl/30/4/10.1063/1.89335>.
- Markus Aspelmeyer, Tobias Kippenberg, and Florian Marquardt. Cavity Optomechanics. *ArXiv e-prints*, 2013.
- P. F. Barker and M. N. Shneider. Cavity cooling of an optically trapped nanoparticle. *Physical Review A*, 81(2):023826, February 2010. ISSN 1050-2947. doi: 10.1103/PhysRevA.81.023826. URL <http://link.aps.org/doi/10.1103/PhysRevA.81.023826>.
- S. A. Beresnev, V. G. Chernyak, and G. A. Fomyagin. Motion of a spherical particle in a rarefied gas. Part 2. Drag and thermal polarization. *Journal of Fluid Mechanics*, 219(-1):405, April 2006. ISSN 0022-1120. doi: 10.1017/S0022112090003007. URL http://journals.cambridge.org/abstract_S0022112090003007.
- Jasper Chan, T P Mayer Alegre, Amir H Safavi-Naeini, Jeff T Hill, Alex Krause, Simon Gröblacher, Markus Aspelmeyer, and Oskar Painter. Laser cooling of a nanomechanical oscillator into its quantum ground state. *Nature*, 478(7367):89–92, October 2011. ISSN 1476-4687. doi: 10.1038/nature10461. URL <http://dx.doi.org/10.1038/nature10461>.
- D E Chang, C A Regal, S B Papp, D J Wilson, J Ye, O Painter, H J Kimble, and P Zoller. Cavity opto-mechanics using an optically levitated nanosphere. *Proceedings of the National Academy of Sciences*, 107(3):1005–1010, 2010. doi: 10.1073/pnas.0912969107. URL <http://www.pnas.org/content/107/3/1005.abstract>.
- M.J.F. Dignonnet, G.S. Kino, H.K. Kim, and S. Fan. Understanding air-core photonic-bandgap fibers: analogy to conventional fibers. *Journal of Lightwave Technology*, 23(12):4169–4177, December 2005. ISSN 0733-8724. doi: 10.1109/JLT.2005.859406. URL <http://ieeexplore.ieee.org/articleDetails.jsp?arnumber=1566743>.
- B. T. Draine. The discrete-dipole approximation and its application to interstellar graphite grains. *The Astrophysical Journal*, 333:848, October 1988. ISSN 0004-637X. doi: 10.1086/166795. URL <http://adsabs.harvard.edu/abs/1988ApJ...333..848D>.
- A. Einstein. Über die von der molekularkinetischen Theorie der Wärme geforderte Bewegung von in ruhenden Flüssigkeiten suspendierten Teilchen. *Annalen der Physik*, 322(8):549–560, 1905. ISSN 00033804. doi: 10.1002/andp.19053220806. URL <http://doi.wiley.com/10.1002/andp.19053220806>.
- T. G. Euser, G. Whyte, M. Scharrer, J. S. Y. Chen, A. Abdolvand, J. Nold, C. F. Kaminski, and P. St. J. Russell. Dynamic control of higher-order modes in hollow-core photonic crystal fibers. *Optics Express*, 16(22):17972, October 2008. ISSN 1094-4087. doi: 10.1364/OE.16.017972. URL <http://www.opticsexpress.org/abstract.cfm?URI=oe-16-22-17972>.

- FEDIAF. Facts and Figures 2012, 2012. URL http://www.fediaf.org/fileadmin/user_upload/Secretariat/facts_and_figures_2012.pdf.
- Stefan Gerlich, Sandra Eibenberger, Mathias Tomandl, Stefan Nimmrichter, Klaus Hornberger, Paul J Fagan, Jens Tüxen, Marcel Mayor, and Markus Arndt. Quantum interference of large organic molecules. *Nature communications*, 2:263, January 2011. ISSN 2041-1723. doi: 10.1038/ncomms1263. URL <http://dx.doi.org/10.1038/ncomms1263>.
- Gian Ghirardi, Philip Pearle, and Alberto Rimini. Markov processes in Hilbert space and continuous spontaneous localization of systems of identical particles. *Physical Review A*, 42(1):78–89, July 1990. ISSN 1050-2947. doi: 10.1103/PhysRevA.42.78. URL <http://link.aps.org/doi/10.1103/PhysRevA.42.78>.
- Jan Gieseler. *Dynamics of optically levitated nanoparticles in high vacuum*. PhD thesis, ICFO, 2013.
- Jan Gieseler, Bradley Deutsch, Romain Quidant, and Lukas Novotny. Subkelvin Parametric Feedback Cooling of a Laser-Trapped Nanoparticle. *Physical Review Letters*, 109(10):103603, September 2012. ISSN 0031-9007. doi: 10.1103/PhysRevLett.109.103603. URL <http://link.aps.org/doi/10.1103/PhysRevLett.109.103603>.
- Domenico Giulini and André Groß ardt. Gravitationally induced inhibitions of dispersion according to the Schrödinger-Newton equation. *Classical and Quantum Gravity*, 28(19):195026, October 2011. ISSN 0264-9381. doi: 10.1088/0264-9381/28/19/195026. URL <http://arxiv.org/abs/1105.1921>.
- David Grass. Optical Trapping and Transport of Nanoparticles with Hollow Core Photonic Crystal Fibers. Master’s thesis, University of Vienna, 2013.
- Klaus Hornberger, Stefan Gerlich, Philipp Haslinger, Stefan Nimmrichter, and Markus Arndt. Colloquium. *Rev. Mod. Phys.*, 84(1):157–173, February 2012. doi: 10.1103/RevModPhys.84.157. URL <http://link.aps.org/doi/10.1103/RevModPhys.84.157>.
- John David Jackson. *Classical electrodynamics*. Wiley, New York, {NY}, 3rd ed. edition, 1999. ISBN 9780471309321. URL <http://cdsweb.cern.ch/record/490457>.
- Nikolai Kiesel, Florian Blaser, Uroš Delić, David Grass, Rainer Kaltenbaek, and Markus Aspelmeyer. Cavity cooling of an optically levitated submicron particle. *Proceedings of the National Academy of Sciences of the United States of America*, 110(35):14180–5, August 2013. ISSN 1091-6490. doi: 10.1073/pnas.1309167110. URL <http://www.pnas.org/content/early/2013/08/08/1309167110.abstract>.
- H Kogelnik and T Li. Laser beams and resonators. *Applied optics*, 5(10):1550–67, October 1966. ISSN 0003-6935. doi: 10.1364/AO.5.001550. URL <http://ao.osa.org/abstract.cfm?URI=ao-5-10-1550>.
- Tongcang Li. *Fundamental Tests of Physics with Optically Trapped Microspheres*. Dissertation, The University of Texas at Austin, 2011.
- Tongcang Li, Simon Kheifets, and Mark G Raizen. Millikelvin cooling of an optically trapped microsphere in vacuum. *Nat Phys*, 7(7):527–530, 2011. URL <http://dx.doi.org/10.1038/nphys1952>.

- Onofrio M Marago, Philip H Jones, Pietro G Gucciardi, Giovanni Volpe, and Andrea C Ferrari. Optical trapping and manipulation of nanostructures. *Nat Nano*, 8(11):807–819, 2013. URL <http://dx.doi.org/10.1038/nnano.2013.208>.
- E. a. J. Marcatili and R. a. Schmeltzer. Hollow Metallic and Dielectric Waveguides for Long Distance Optical Transmission and Lasers. *Bell System Technical Journal*, 43(4):1783–1809, July 1964. ISSN 00058580. doi: 10.1002/j.1538-7305.1964.tb04108.x. URL <http://doi.wiley.com/10.1002/j.1538-7305.1964.tb04108.x>.
- J Nold, P Hölzer, N Y Joly, G K L Wong, A Nazarkin, A Podlipensky, M Scharrer, and P St J Russell. Pressure-controlled phase matching to third harmonic in Ar-filled hollow-core photonic crystal fiber. *Optics letters*, 35(17):2922–4, September 2010. ISSN 1539-4794. doi: 10.1364/OL.35.002922. URL <http://ol.osa.org/abstract.cfm?URI=ol-35-17-2922>.
- Lukas Novotny. Private communication.
- Lukas Novotny and Bert Hecht. *Principles of Nano-Optics*. Cambridge University Press, 2006. URL <http://www.cambridge.org/at/academic/subjects/physics/optics-optoelectronics-and-photonics/principles-nano-optics?format=HB>.
- A D O’Connell, M Hofheinz, M Ansmann, Radoslaw C Bialczak, M Lenander, Erik Lucero, M Neeley, D Sank, H Wang, M Weides, J Wenner, John M Martinis, and A N Cleland. Quantum ground state and single-phonon control of a mechanical resonator. *Nature*, 464(7289):697–703, April 2010. ISSN 1476-4687. doi: 10.1038/nature08967. URL <http://dx.doi.org/10.1038/nature08967>.
- T A Palomaki, J D Teufel, R W Simmonds, and K W Lehnert. Entangling mechanical motion with microwave fields. *Science (New York, N.Y.)*, 342(6159):710–3, November 2013. ISSN 1095-9203. doi: 10.1126/science.1244563. URL <http://www.sciencemag.org/content/342/6159/710>.
- Roger Penrose. On Gravity’s role in Quantum State Reduction. *General Relativity and Gravitation*, 28(5):581–600, May 1996. ISSN 0001-7701. doi: 10.1007/BF02105068. URL <http://link.springer.com/10.1007/BF02105068>.
- Oriol Romero-Isart, Mathieu L Juan, Romain Quidant, and J Ignacio Cirac. Toward quantum superposition of living organisms. *New Journal of Physics*, 12(3):33015, 2010. URL <http://stacks.iop.org/1367-2630/12/i=3/a=033015>.
- Philip Russell. Photonic crystal fibers. *Science (New York, N.Y.)*, 299(5605):358–62, January 2003. ISSN 1095-9203. doi: 10.1126/science.1079280. URL <http://www.sciencemag.org/content/299/5605/358>.
- Philip St.J. Russell. Photonic-Crystal Fibers. *Journal of Lightwave Technology*, 24(12):4729–4749, December 2006. URL <http://www.opticsinfobase.org/abstract.cfm?uri=jlt-24-12-4729>.
- Bahaa E A Saleh and Malvin Carl Teich. *Fundamentals of Photonics; 2nd ed.* Wiley series in pure and applied optics. Wiley, New York, NY, 2007. URL <http://cds.cern.ch/record/1084451?ln=de>.

- Oliver A Schmidt, Tijmen G Euser, and Philip St J Russell. Mode-based microparticle conveyor belt in air-filled hollow-core photonic crystal fiber. *Optics express*, 21(24):29383–91, December 2013. ISSN 1094-4087. doi: 10.1364/OE.21.029383. URL <http://www.opticsexpress.org/abstract.cfm?URI=oe-21-24-29383>.
- Statistik Austria. Ergebnisse im Überblick: Privathaushalte 1985 - 2013, 2014. URL http://www.statistik.at/web_de/statistiken/bevoelkerung/haushalte_familien_lebensformen/haushalte/index.html.
- J D Teufel, T Donner, Dale Li, J W Harlow, M S Allman, K Cicak, A J Sirois, J D Whittaker, K W Lehnert, and R W Simmonds. Sideband cooling of micromechanical motion to the quantum ground state. *Nature*, 475(7356):359–63, July 2011. ISSN 1476-4687. doi: 10.1038/nature10261. URL <http://dx.doi.org/10.1038/nature10261>.
- G. Uhlenbeck and L. Ornstein. On the Theory of the Brownian Motion. *Physical Review*, 36(5):823–841, September 1930. ISSN 0031-899X. doi: 10.1103/PhysRev.36.823. URL <http://link.aps.org/doi/10.1103/PhysRev.36.823>.
- Kiarash Zamani Aghaie, Vinayak Dangu, Michel J. F. Digonnet, Shanhui Fan, and Gordon S. Kino. Classification of the Core Modes of Hollow-Core Photonic-Bandgap Fibers. *IEEE Journal of Quantum Electronics*, 45(9):1192–1200, September 2009. ISSN 0018-9197. doi: 10.1109/JQE.2009.2019767. URL <http://ieeexplore.ieee.org/lpdocs/epic03/wrapper.htm?arnumber=5226781>.